



HAL
open science

Recent Progresses in Metal–Organic Frameworks Based Core–shell Composites

Shan Dai, Antoine Tissot, Christian Serre

► **To cite this version:**

Shan Dai, Antoine Tissot, Christian Serre. Recent Progresses in Metal–Organic Frameworks Based Core–shell Composites. *Advanced Energy Materials*, In press, pp.2100061. 10.1002/aenm.202100061 . hal-03403562

HAL Id: hal-03403562

<https://hal.science/hal-03403562>

Submitted on 26 Oct 2021

HAL is a multi-disciplinary open access archive for the deposit and dissemination of scientific research documents, whether they are published or not. The documents may come from teaching and research institutions in France or abroad, or from public or private research centers.

L'archive ouverte pluridisciplinaire **HAL**, est destinée au dépôt et à la diffusion de documents scientifiques de niveau recherche, publiés ou non, émanant des établissements d'enseignement et de recherche français ou étrangers, des laboratoires publics ou privés.

Recent Progresses in Metal-Organic Frameworks based core-shell composites

Shan Dai, Antoine Tissot, Christian Serre**

S. Dai, Dr. A. Tissot, Dr. C. Serre
Institut des Matériaux Poreux de Paris, Ecole Normale Supérieure, ESPCI Paris, CNRS, PSL
University, 75005, Paris, France

E-mail: antoine.tissot@ens.psl.eu; christian.serre@ens.psl.eu

Keywords: Core-shell, Metal-organic frameworks, Catalysis, Environmental applications

Abstract: Encapsulation of active guest compounds inside Metal-Organic Frameworks (MOFs) architectures is one of the most promising routes to reach properties beyond those of the bare MOFs and/or guest species. In contrast with the conventional host/guest composites that rely on the encapsulation of guest species into MOF cavities, core-shell composites display a better accessibility to the pores ensuring an optimal diffusion of the substrate while presenting a unique structure that prevents from the aggregation and the runoff of the active guests and ensures a tight interaction between core and shell, leading to synergistic effects. Herein, this progress report summarizes the recent advances in this field. The main synthetic strategies are first discussed before highlighting few potential applications, such as heterogeneous environmental catalysis, gas separation and sensing, while others (bio-applications...) will be briefly mentioned. We conclude this review by a critical perspective in order to promote new generations of MOFs based composites for energy-related applications.

1. Introduction

Metal-organic frameworks (MOFs) are a class of crystalline porous hybrid materials with varying dimensionality that has been widely studied in the past two decades.^[1] MOFs properties mainly derive from the structural arrangements of their inorganic part (metal cations, eventually assembled in secondary building units (SBUs)) with organic ligands.^[2] The high degree of tuneability of these solids, including pre-design and post-modification approaches, makes MOFs appealing for various potential applications,^[3] particularly in the field of energy.^[4] Compared to conventional porous solids (e.g. Metal oxides, Zeolites, Carbon materials. etc), MOFs can exhibit an unprecedented diversity in terms of pore sizes and shapes, associated in some cases to remarkable surface areas (up to 7000 m²/g,^[5] BET model) and/or redox or Lewis open metal sites (OMS).^[7] Noteworthy MOFs can also benefit from an easy ligand functionalization towards the enhancement of their catalytic properties, including the concepts of “multivariate MOFs”.^[6] Incorporating guest moieties into MOFs presents a great potential for several applications (e.g. catalysis, gas separation), as the encapsulated guest materials can introduce new requested properties that are absent in the parent material. In addition, the properties of the composite may outperform the one of each single component.^[7, 8] Well-documented synthetic strategies have been reported, including pre- and post-synthetic guest incorporation, depending on the interaction between the host and the guest.^[9] For example, a wide range of functional materials (e.g. inorganic metal nanoparticles, coordination complexes, quantum dots, polyoxometalates, enzymes, and polymers...) have been introduced post-synthetically into the pores of MOFs.^[10, 11] Among them, inorganic metal nanoparticles (NPs) have been widely studied due to their remarkable properties in energy and environmentally-related applications.^[4] The features of these MOF-based composites make them appealing to address prominent issues in catalysis.^[12] Nevertheless, there are still several limitations that still need to be considered: (1) the confined nanoparticles can block the pores during their growth, therefore preventing the substrate from diffusing inside the solid; (2) only guest species smaller than the pore dimensions can be loaded; (3) in some cases, the shape/ morphology of the guest species cannot be controlled due to constraints imposed by the host (pore shape/size/interactions...); (4) the precise control of the guest location is in most cases not possible and depositing guests on the MOF external surface is unavoidable, regardless of very limited tentative studies;^[13, 14] (5) guests may leach in liquid phase, leading to unwanted homogeneous catalysis. In order to overcome these problems, the preparation of core-shell compounds using MOFs was first proposed in 2012.^[10, 15] This so-called “bottle-around-ship” strategy is based on the construction of a stratified structure, where the “core” (that can be inorganic nanoparticles,^[16] MOFs,^[17] Metal oxides,^[18] Silica,^[19] Polymers,^[20] Carbon nanotubes,^[21] etc) is encased in a MOF “shell”. It allows an effective encapsulation regardless the shape, size, morphology, and composition of the “core”. For example, one MOF can cover a second MOF, forming a MOF@MOF architecture, which greatly expands the accessible structural complexity.^[8, 22, 23] Notably, thanks to complementary chemical/physical properties, the combination of two distinct materials might lead to the synergetic effect, where the resulting core-shell structure behaves beyond each single material.^[24, 25] Lately, researchers have started to pay attention on derived composites based on core-shell MOF-based architectures for advanced applications. Of those, carbonized core-shell composites and hollow structures (yolk-shell,^[26] hollow multi-shelled structures^[27, 28]) particularly exhibited

broad research interest due to their promising properties (conductivity,^[29] hierarchical porosity,^[30] diffusion,^[31] etc.). Note that for the carbonized compounds, even though the thermolysis at high temperature often destroy the MOFs, the overall remaining porosity and the sequence of active sites can often be maintained. Concerning the yolk-shell or hollow structures, they can be obtained starting from pre-formed core-shell structures thanks to the differences in the chemical/physical stability between core and shell that provides the opportunity to perform a controllable etching of the core materials.^[32] However, due to the limited scope of this review and the recently published ones on this topic,^[33] we will not present here derived materials based on core-shell composites.

In this report, we summarize the most significant recent progresses in the development of core-shell NPs@MOF and MOF@MOF, with a particular emphasis on the synthetic strategies and synergistic effects. In the first case, MOFs are not only playing the role of supports to host NPs, which effectively prevents their aggregation during the material preparation and use, but also give a fully available pore space required for an optimal diffusion of the substrates. In the second case, whose development is even more recent, most studies refer to gas separation, probably due to the possibility to combine the properties of the two materials (e.g. uptake and selectivity) in order to get optimized sorption behaviour. Finally, we will propose perspectives for the design of new generations of advanced core-shell composites for diverse applications such as energy-related catalysis and gas separation.



Scheme 1. Illustration of the synthetic methods (CAAS = Capping agent-assisted synthesis; ITAS = Inorganic template-assisted synthesis; EGS = Epitaxial growth synthesis) and the main applications of core-shell MOFs based composites.

2. Synthetic methods of core-shell MOF-based composites

2.1. Capping agent-assisted synthesis

The capping agent-assisted synthesis (CAAS) usually involves two steps, where the pre-synthesized core material is first prepared prior to the growth of MOF shell around, resulting in discrete species within the ordered MOF framework. However, the preparation of core-shell MOF-based composites still remains challenging due to the risk of aggregation of active NPs and/or of self-nucleation of MOF particles. Capping agents/surfactants can to some extent prevent this, on one hand inhibiting the aggregation of small NPs and on the other hand compensating the lattice mismatch between the MOF and the NPs. In a pioneering work, Lu et al. reported a versatile polyvinylpyrrolidone (PVP) assisted approach to encapsulate several inorganic materials with distinct sizes and shapes in ZIF-8 (ZIF stands for Zeolitic Imidazolate Frameworks), which subsequently led to a catalytic/physical properties enhancement. Transmission electron microscopy (TEM) suggested that the encapsulation process does not rely on the heterogeneous nucleation mechanism, but instead is based on the continuous growth of a MOF shell around the particles. In the synthesis process, PVP not only contributes to the stability of the inorganic nanoparticles but also enhances its affinity with the coordination-polymer through weak interactions, either between pyrrolidone rings (C=O) and Zn(II) ions from ZIF nodes and/or between apolar groups of PVP and the organic linkers of the MOF.^[10]

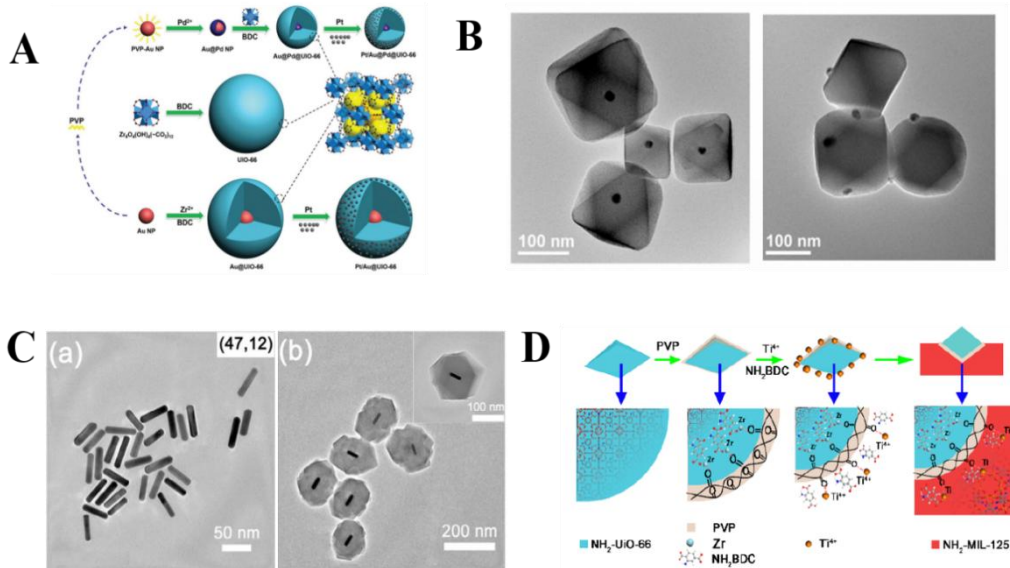


Figure 1. A) Synthetic route for the synthesis of Au@Pd NPs and other composites. B) TEM images of Cu nanocrystals embedded into UiO-66 and Cu nanocrystals on the external surface of UiO-66. C) TEM images of CTAB-stabilized Au NRs (a) and TEM image of Au NRs@ZIF-8 core-shell nanostructure (b). D) Schematic representations of the coordination phenomenon associated with the systematic growth of the MOF-on-MOF hybrid structure. A-D) Reproduced with permission.^[34-37] Copyright 2018, Wiley-VCH. Copyright 2016, American Chemical Society. Copyright 2018, Springer.

Since then, CAAS method have been used with a broad range of compounds, including bimetallic alloys, non-noble metal NPs, NPs with various shapes/ sizes, as well as using MOF as core. PVP, an amphiphilic non-ionic polymer of a low toxicity, is one of the most common capping agent for encapsulation of inorganic materials in MOFs. For example, Hu et al. used PVP protected Au NPs and Au@Pd bimetallic NPs to fabricate monodisperse spherical core-shell architectures with UiO-66 (Figure 1A).^[34] The accessible pore space enabled an additional encapsulation of Pt NPs through conventional ship-in-a-bottle strategy. In addition to noble metal NPs, Yaghi et al. reported single 18 nm PVP coated Cu nanocrystals encapsulated within UiO-66 single crystals and 18 nm Cu nanocrystals anchored on the external surface of UiO-66 crystals (Figure 1B).^[35] The resulting Cu nanocrystal@UiO-66 exhibited a superior catalytic activity in comparison with the Cu nanocrystals deposited on the outer surface of the MOF. In addition, the use of Zr(OiPr)₄ as precursor for the MOF synthesis led to a better core-shell structure compared with the use of acidic salts such as ZrCl₄ and ZrOCl₂ due to the possible dissolution of Cu nanocrystals under acidic conditions. Similarly, Tang et al. encapsulated PVP-stabilized Au Nanorods (Au NRs) in ZIF-8 using a two steps method (Figure 1C). The well-defined single Au NRs@ZIF-8 particles showed preserved porosity and high purity, paving the way for optical studies on these anisotropic objects.^[36] Other works also reported the encapsulation of other inorganic materials with distinct morphologies,^[27] shapes^[38] and sizes^[39]. Apart from inorganic nanomaterials, Kitagawa et al. proposed a general strategy for the synthesis of MOF@MOF hetero-architectures where PVP was used to overcome the limitation of the lattice matching rule (Figure 1D).^[37] The PVP played a role like glue, interacting with the core metal (Zr⁴⁺) in the first step via electrostatic attraction and then coordinating to the shell metal cations (Ti⁴⁺), therefore giving a chance to combine 3D MOFs that have distinct topologies. In addition, the authors demonstrated that the sizes and morphologies of MOF crystals can be well controlled by changing the amount of PVP and of core MOF particles.

In addition to polymers, CAAS was also intensively applied using other kinds of small molecules / surfactants depending on the capping agent requested in the design process of core materials.^[40] For example, cetyltrimethylammonium bromide (CTAB) is a surfactant that enables individual encasement and controlled alignment of several nanomaterials.^[41, 42] Yang et al. applied CTAB as a bridging layer to construct a series of MOF-based core-shell/yolk-shell structures on the surface of Pt-Ni nanoframes through the sequence of encasement, overgrowth, and dissociation of the sacrificed shell.^[43] The sizes and shapes of the final composite could be tuned by changing the growth time and the quantity of CTAB in solution. In another example, the hydrophobic tail of CTAB was used to control the interaction between Pd particles and ZIF-8 in order to align the (100) planes of Pd structure with the (110) planes of ZIF-8.^[44] Tsung et al. also reported a core-shell UiO-66@ZIF-8 structure using CTAB as a surfactant. The CTAB was proven to be the optimal surfactant in terms of shape/overgrowth control in comparison with other micelle forming surfactants, such as tetradecyltrimethylammonium bromide (TTAB), cetylpyridinium bromide (CPB), and sodium dodecyl sulfate (SDS), as well as with PVP. It is worth noticing (Figure 2E) that the thickness of the MOF shell can be tuned down to 40 nm depending on the amount of reactants used.^[45] Dang et al. presented a facile LYZ (self-assembled lysozymes)-based strategy (Figure 2B) for fabricating well-defined core-shell nanocomposites consisting of a NP core and a MOF shell. The LYZs could spontaneously form a robust layer with abundant functional groups on the surfaces of NPs such as 14 nm Au NPs, Au nanostars, CdTe quantum dots, CuO, β -FeOOH, magnetic NPs (Figure 2C), which makes them handy to mediate the MOFs heterogeneous nucleation and growth at their surface.^[46] Hence, use

of a stronger capping agent can be a useful approach to create core-shell NP@MOF nanocomposites due to its high affinity with both NPs and MOF.

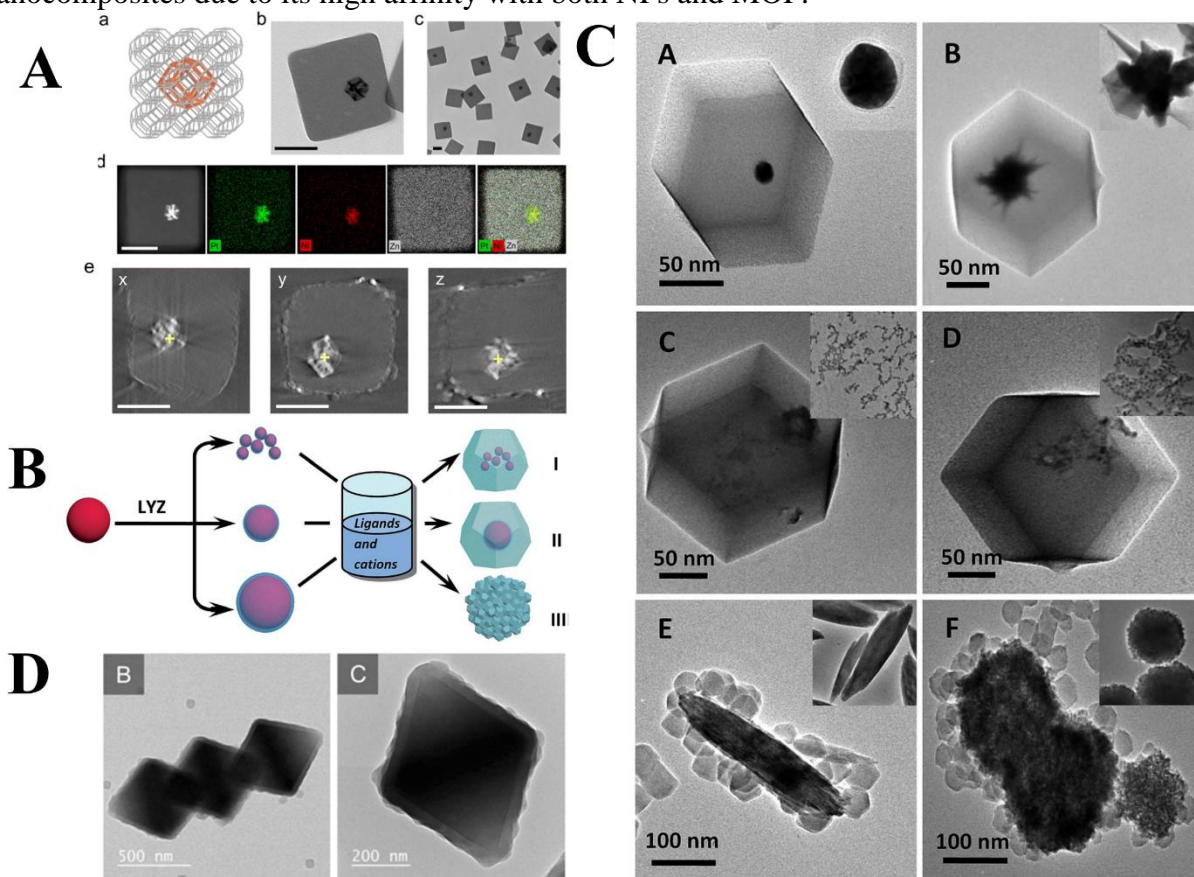


Figure 2. A) Scheme of the Pt-Ni@ZIF-8 core-shell composites (a), TEM images of the obtained composites (b-c), HAADF-STEM image and EDX maps (d), tomographic reconstruction images of single core-shell frame-in-frame structure, the yellow plus marker shows the same position in all three orthogonal slices (e). B) Illustration of the stepwise strategy of the controlled encapsulation of NPs in ZIF-8 to form multiple- (I) or single-core-monocrystalline-shell (II) or single-core-polycrystalline-shell (III) structures. C) TEM images of Nanoparticles@ZIF-8 ((a-f) with various core materials (14 nm Au NPs, Au nanostar, CdTe, CuO, β -FeOOH, MNP) D) TEM images of UiO-66@ZIF-8. Reproduced with permission.^[43, 45, 46] Copyright 2020, American Chemical Society. Copyright 2017, Royal Society of Chemistry. Wiley-VCH. Copyright 2015, Wiley-VCH.

2.2. Inorganic template-assisted synthesis

Inorganic template-assisted synthesis (ITAS) is a core-shell fabrication process that involves two steps: the binding of inorganic materials with core materials, such as coating with SiO_2 (serving as binding sites for shell MOF) or metal oxide (subsequently be used as the metal source for the shell MOF growth) and the MOF synthesis.^[47] The preparation of such core-shell composites has few manifest advantages: 1) the template metal oxide can be directly used as the metal source of shell MOF; 2) in the case of reactive NPs, the particles can be protected by an oxide shell during

the synthesis and might be accessible to catalytic substrates when the shell is fully dissolved. Even though the ITAS method looks appealing, it exhibits some disadvantages in comparison with CAAS method such as the limited designability of the wrapped NPs (size, shape, morphology, etc.) associated with the necessary shell MOF chemical stability when the etching of the sacrificing metal oxide is needed as well as the request of an easy to dissolve sacrificing metal oxide. Pioneering works have used ZnO,^[48] Cu₂O,^[49] Al₂O₃^[50], Silica^[51] as a template for the construction of core-shell composites. Recently, Cheng et al. coated Cu₂O particles with silica, which were further encapsulated into ZIF-8, representing the first room temperature incorporation of unstable active Cu₂O nanocubes within a MOF (Figure 3A-C). A blue slurry was obtained instead of yellow one when SiO₂ was not used as protective layer (Figure 3C), confirming the role of SiO₂ to avoid Cu(I) oxidation. In addition to being a useful protective layer, SiO₂ can also play a role as sacrificial template to form a hollow structure (40nm in size) when selective etching of SiO₂ is performed using NaOH under inert atmosphere.^[52] Metal oxide/ Metal(0) nanoparticles have also been used as sacrificing agents to form core-shell architectures.^[53, 54] For example, Che et al. synthesized nanostructures of the octahedron and flower Pt-Cu@HKUST-1, where Pt-Cu alloys acted as a template for the subsequent MOF shell growth in-situ via the consumption of Cu(0). In a typical synthesis, Pt-Cu alloy with various morphologies were pre-synthesized (Figure 3D, schematic illustration) and PVP was used as capping agent for protecting active Pt-Cu alloy while Fe(III) was used in order to oxidize Cu(0) in Cu(II). Pt-Cu with different morphologies were encapsulated in HKUST particles (Figure 3E (a-b)), evidencing the versatility of the ITAS method. The obtained octahedron and flower Pt-Cu@HKUST-1 both presented a very thin shell thickness of ca. 21- 25 nm and almost unchanged Pt-Cu alloy size (ca. 43nm).^[54]

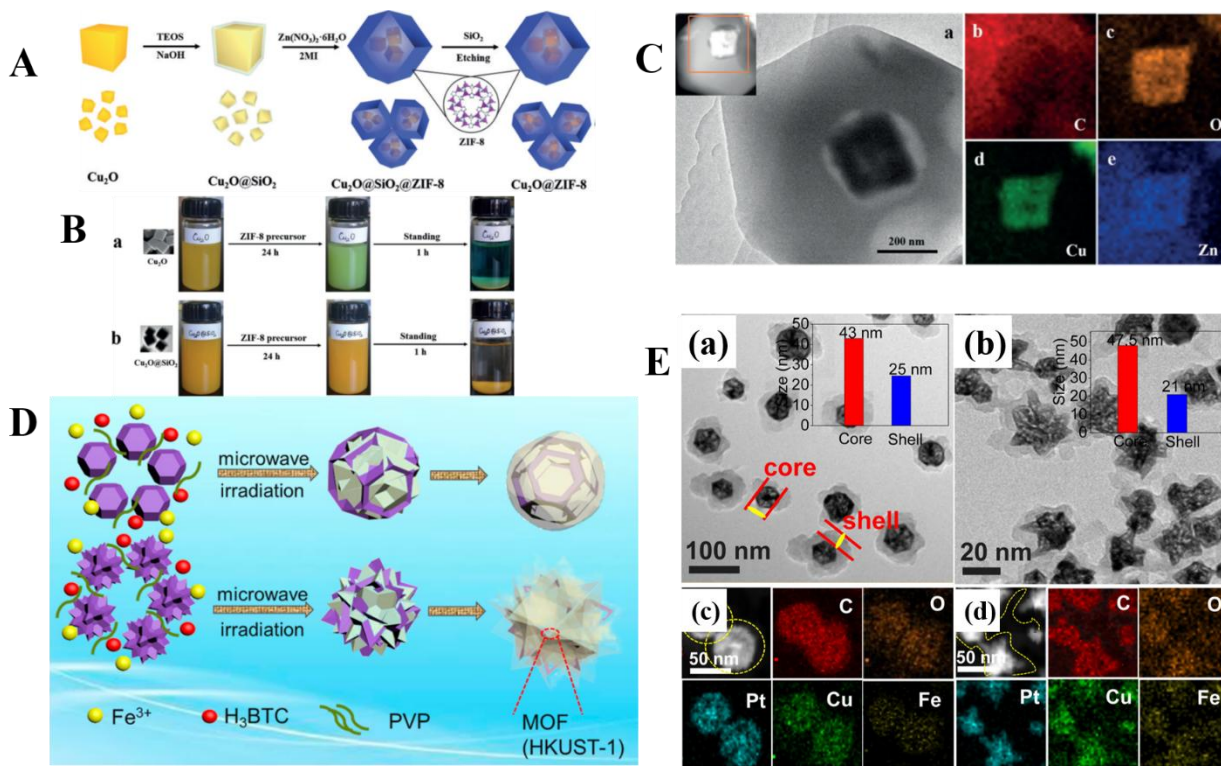


Figure 3. A) Schematic illustration for the synthesis of Cu₂O@ZIF-8 composites. B) Comparative experiment for the stability of (a) Cu₂O and (b) Cu₂O@SiO₂. C) (a) TEM image of Cu₂O@ZIF-8, (b-e) elemental distribution for Cu₂O@ZIF-8. D) Illustration of the in-situ synthesis of Pt-Cu frame@HKUST-1 under the Microwave irradiation TSS method. E) (a-b) TEM images of octahedron Pt-Cu frame@HKUST-1 and flower Pt-Cu frame@HKUST-1 (insert: size distribution histogram). Reproduced with permission.^[52, 54] Copyright 2018, Wiley-VCH. Copyright 2017, American Chemical Society.

2.3. One-pot synthesis

One-pot synthesis consists in a direct mixing of both MOFs and NPs precursors in one pot.^[55] It exhibits serious advantages such as high efficiency, low complexity, and upscaling ability. It should be pointed out that the active cation for the NPs synthesis should undergo few steps in the presence of MOF precursors in solution (metal source, ligand) that are, the reduction into metal particle, the protection of the NPs, followed by the MOF growth around the NPs. Therefore, solvothermal conditions for MOFs synthesis are usually not compatible with this strategy due to a lack of control of the formation of the inorganic NPs. This raises additional challenges for the MOF chemists. Li's group reported first the one-step synthesis of Pt NPs@UiO-66 where H₂ and DMF were used as reducing and bridging agents, respectively. The specific interactions between Pt⁰ and -C-N groups and between C=O moieties and Zr⁴⁺ favored the growth of the MOF on the surface of Pt NPs rather than in solution.^[14] More recently, Wang et al. reported a one-pot PVP microwave irradiation-assisted strategy to fabricate Ag NPs@IRMOF-3 (illustrated in Figure 4A).^[56] This facile synthesis procedure allowed a fine control of the shell thickness (Figure 4B (a-c)) from 24 nm to 175 nm simply through a control of the reaction time. The size of Ag NPs could also be tuned by decreasing the initial concentration of AgNO₃ (Figure 4B (b, d, e)) and increasing the amount of PVP, leading to a size down to 5.2 nm with the lowest Ag loading. Indeed, PVP acted as a stabilizer of Ag NPs as well as provided interactions to adsorb IRMOF-3 precursors onto the Ag NPs surfaces via coordination interaction between the pyrrolidone rings (C=O) and Zn²⁺. In this work, the heating method seemed to be key point, as the use of solvothermal heating led to self-depositing of small Ag NPs rather than to a core-shell structure.

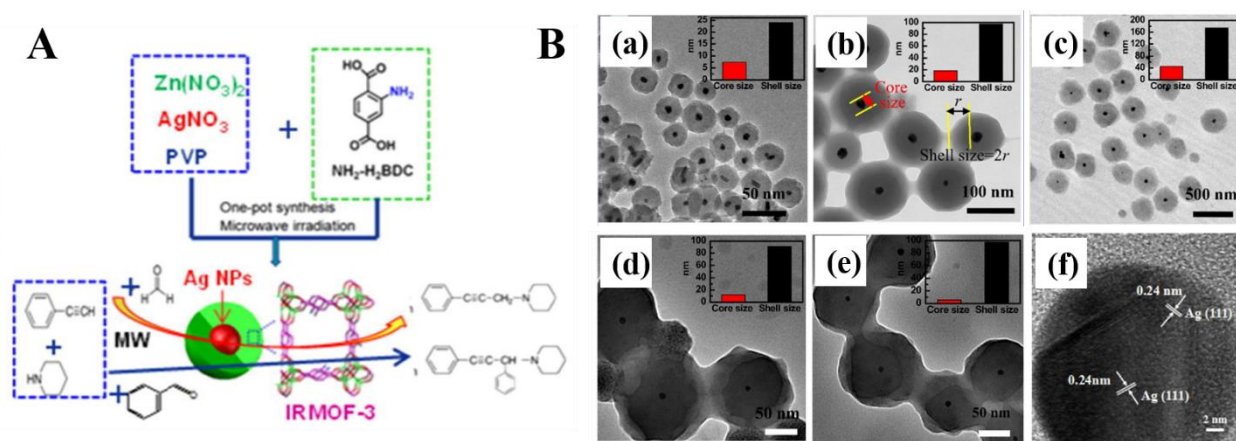


Figure 4. A) Schematic illustration for the synthesis of one-pot Ag NPs@IRMOF-3. B) TEM images and average sizes of core and shell (inset) of Ag@IRMOF-3 nanostructures under MW

heating at 120 °C with 0.014 mmol AgNO₃ at crystallization time of (A) 5 min, (B) 15 min, (C) 30 min, and with (D) 0.0014 mmol, (E) 0.0005 mmol AgNO₃ at crystallization time of 15 min, (F) HRTEM image of the represented core. Reproduced with permission.^[56] Copyright 2017, Elsevier Inc.

2.4. Epitaxial growth synthesis

Epitaxial growth synthesis (EGS) involves the synthesis of the core MOF particle followed by the fabrication of the second layer of MOF around the core.^[17, 57] It should be noted that the shell “MOF” usually have to exhibit a similar topology than core one. In addition, active NPs can be deposited/ adsorbed at the interface of the two layers before the epitaxial growth. The compounds MOFs@NPs@MOFs are also called sandwich structures. Such composites have many similarities to conventional core-shell structures, while the control of the shell thickness in the super-thin range (<10 nm) is easier due to the great synthetic flexibility accessible for the shell synthesis (tuning the concentration of precursors, reactants ratio...). Tang et al. reported a series of sandwich structures based on MIL-101 and Pt NPs in 2016, which represent a proof of concept to design highly efficient and selective catalysts.^[58] Recently, this group synthesized a series of sandwich structures UiO-67@Pd NPs@UiO-X (X=66, 67(N) (N = 2,2'-bipyridine-5,5'-dicarboxylic acid), 67, 68) to study the contribution of organic linkers in catalytic efficiency via a similar epitaxial growth method (Figure 5 (A)). Micron-scale UiO-67 was chosen as the core and pre-synthesized in DMF through a conventional method (Figure 5 (B, C)). In a second step, H₂PdCl₄ was added to UiO-67 dispersed in methanol and reduced by NaBH₄. Figure 5 (D, E) demonstrated that the ultra-small Pd NPs were deposited on the surface of the MOF crystals. Subsequently, the precursors of the shell were mixed with the UiO-67@Pd suspension and the core-shell structure was formed after solvothermal synthesis. Figure 5 (F, G) evidences the ideal spatial distribution of Pd NPs, with a shell thickness that is controllable from 35 to 50 nm by optimizing the precursor concentration and coating time. Additionally, other shells including UiO-66, UiO-67(N), and UiO-68 were also produced.^[59] Similarly, in order to overcome the ill-defined MNPs and blurred interactions at the interface, Zhu et al. reported a sandwich MOFs@APNPs@MOFs (APNCs= monodisperse atomically precise nanoclusters) structure, in which the encapsulated Au NCs are Au₂₅(L-Cys)₁₈ clusters.^[60]

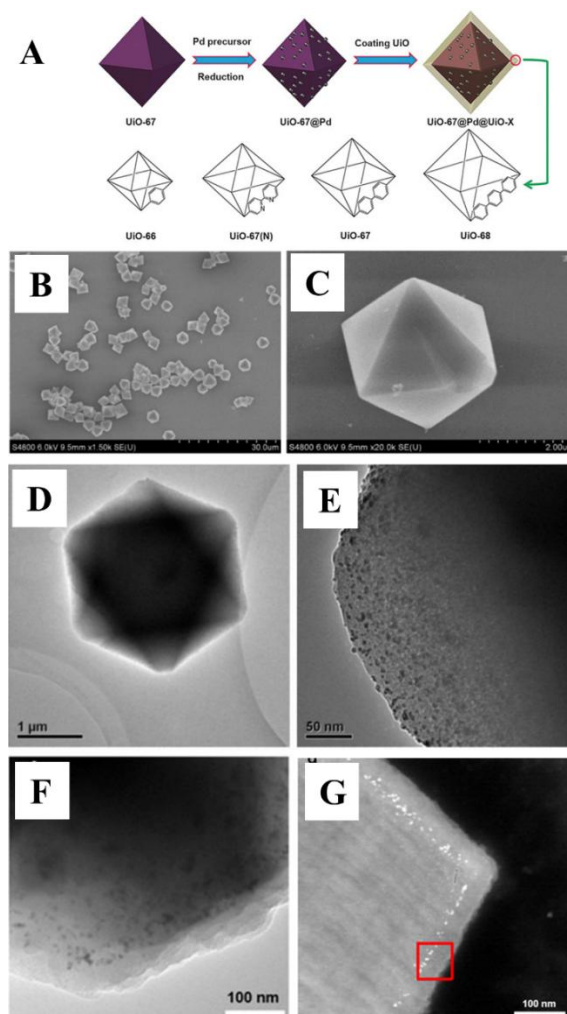


Figure 5. A) Synthetic route of Pd NPs sandwiched by a UiO core and shell with different pore apertures and wettability, UiO@Pd@UiO-X (X=66, 67(N), and 68). B, C) SEM images of UiO-67. D, E) TEM images of single UiO-67@Pd. F) TEM image of UiO-67@Pd@UiO-67 (50 nm). G) HAADF-STEM image of the cross-section of UiO-67@Pd@UiO-67 (50 nm). Reproduced with permission.^[59] Copyright 2019, Wiley-VCH.

Apart from the examples loaded with active NPs, strategies to prepare bare MOFs@MOFs (also called MOF-on-MOF) have also been investigated recently.^[61] In that case, overcoming the large mismatched lattices (for example Fe-MIL-88B@Fe-MIL-88C, illustrated in Figure 6(A)) is challenging, despite the use of isorecticular core and shell. Moonhyun et al. reported the synthesis of core-shell hybrid MOFs with the use of tip-to-middle anisotropic growth method, where the growth of the MOF shell (Fe-MIL-88C) started selectively at the tips of the template and effectively propagated along the *c* direction of core MOF. As shown in Figure 6(B), the pre-synthesized Fe-MIL-88B core exhibits a 3D hexagonal structure with a particle length at $0.88 \pm 0.10 \mu\text{m}$. The MOF growth process was monitored by SEM after 50 s, 80 s, and 600 s (Figure 6 (C-E)), corresponding to the intermediates and final product, respectively. X-ray powder diffraction proved that due to the highly flexible nature of MIL-88's, the cell parameters of Fe-MIL-88C could be self-adjusted according to the template for the effective growth, especially on

the *ab* planes exposed at the particles tips. In a control experiment, the solvothermal reaction of 4, 4'- biphenyldicarboxylic acid (H₂BPDC), and Fe(NO₃)₃ in the presence of pre-formed Fe-MIL-88B particles was performed in order to obtain Fe-MIL-88B@Fe-MIL-88D. However, only independent MOF crystals were formed, indicating this epitaxial growth synthesis may not be suitable for compounds presenting too large lattice mismatches. Nevertheless, a more complex well-defined core-shell of Fe-MIL-88B@Ga-MIL-88B@Fe-MIL-88C was successfully formed (Figure 6(F)), demonstrating the large scope of this anisotropic growth method.^[62]

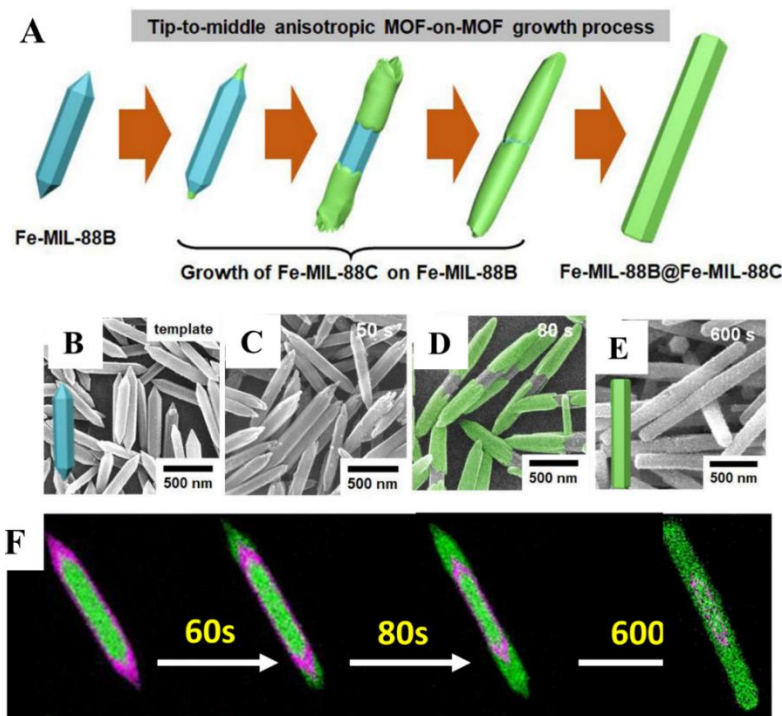


Figure 6. A) Schematic representation for the proposed tip-to-middle anisotropic MOF-on-MOF growth process with mismatched cell lattices for the production of well-defined core-shell hybrid Fe-MIL-88B@Fe-MIL-88C. SEM images monitoring the MOF-on-MOF growth process during the formation of core-shell hybrid Fe-MIL-88B@Fe-MIL-88C, at B) 0 s, C) 50 s, D) 80 s, E) 600 s. Newly grown shells in the intermediates are highlighted in green in D). F) Elemental mapping images monitoring the tip-to-middle anisotropic MOF-on-MOF growth process for the formation of doubly shelled core-shell Fe-MIL-88B@Ga-MIL-88B@Fe-MIL-88C, green color represents Fe, purple color represents Ga. Reproduced with permission^[62]. Copyright 2020, American Chemical Society.

2.5. Discussion

The synthesis of core-shell architectures has experienced a rapid development during last years due to their high potential for applications in catalysis, sensing etc. Among the various strategies, ITAS method is a facile route however facing disadvantages such as the compromise in structure robustness that is needed in order to extract metal ions from the core. Therefore, most studies were focused on divalent-based MOFs and implementing them with more robust metal(III, IV)

MOFs remains an important challenge. CAAS appears as the strategy with the broadest range of utilization due to its ease in controlling the shape, size, and chemical nature of the encapsulated core. However, the presence of multiple steps as well as the use of capping agents might limit its practical use. EGS is a more recent approach that exhibits many similarities to CAAS but can allow the synthesis of super-thin shell thickness, therefore improving the diffusion of the substrates. Recently, work reported by Kwon et al. showed the MOFs that share similar 2D lattice parameters can be used for epitaxial growth, which might help to explore other composites.^[63] Although the above-mentioned methods are considered as more rational approaches and therefore have been commonly used so far, there is still a need to devote more effort to develop one-pot synthesis which, from a practical point of view, looks quite promising due to its lower cost and easier up-scaling.^[64] As a pre-requisite for the incorporation of functional but fragile compounds in chemically stable MOFs, mild synthesis conditions, e.g., relatively low synthesis temperature, eventually down to room temperature, were explored but remain challenging.^[10, 35, 65, 66] For instance, we have reported very recently a versatile one-step room-temperature environmentally-friendly approach for the syntheses of 12-connected (MOF-801, UiO-66-NH₂, UiO-66-COOH) and 8-connected (DUT-67, PCN-222) M₆ oxoclusters (M=Zr, Hf, Ce) based MOFs (Figure 7). The efficient synthetic strategy allows us not only to tune the MOF particles size but also to achieve a high space time yield that could pave the way towards the more effective and efficient construction of core-shell composites.^[67]

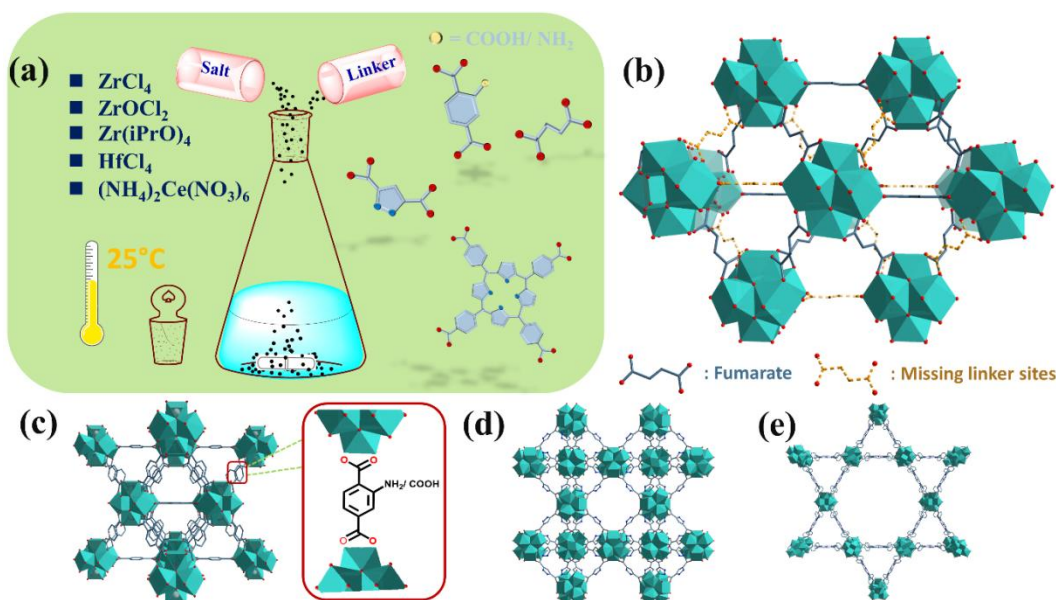


Figure 7. Schematic diagram of the room temperature one-step synthesis approach (a). Representative of the crystal structures of MOF-801(Zr, Hf, Ce) viewed along (101) plane and the illustration of existing defects (b), UiO-66-COOH/ NH₂ (c), DUT-67(PDA) (d) and PCN-222 (e). Metal polyhedra, carbon and oxygen atoms are in cyan, black and red, respectively (hydrogen atoms have been omitted for the sake of clarity). Reproduced with permission.^[57] Copyright 2020, Wiley-VCH.

Table 1. Comparison of the different synthetic methods.

	CAAS (Capping agent-assisted synthesis)	ITAS (Inorganic template-assisted synthesis)	One-pot	EGS (Epitaxial growth synthesis)
Advantages	<ul style="list-style-type: none"> • Most versatile method • Tunable synthetic parameters • Allow large lattice mismatches 	<ul style="list-style-type: none"> • “Clean” surface of NPs 	<ul style="list-style-type: none"> • Direct • Potentially scalable 	<ul style="list-style-type: none"> • “Clean” surface of NPs (sandwich composites) • Tunable shell thickness
Disadvantages	<ul style="list-style-type: none"> • Remaining bridging agent that may block the active sites • Multiple-steps synthesis 	<ul style="list-style-type: none"> • Limited core and shell candidates (shape, morphology, size) • Relative low chemical stability of the shell MOF • Multiple-steps synthesis 	<ul style="list-style-type: none"> • Remaining capping agent • Challenging synthesis • Lack of properties control 	<ul style="list-style-type: none"> • Similar structure needed for core and shell (MOF@MOF) • More complex synthesis (sandwich composites)

3. Characterizations of core-shell MOF-based composites

One important challenge for the core-shell MOFs materials is to precisely determine the location and spatial distribution of the core materials, particularly in the following cases: 1) ultra-small NPs (diameter ≤ 3 nm) where it is often hard to distinguish if the NPs are located inside or on the MOF surface; 2) light metal NPs (such as Cu NPs, Fe/ Fe_xO_y NPs. etc) that suffer from a lack of electron density contrast when combined with heavy metal-based MOF shells (e.g. Zr, Hf, etc.)^[68, 69]; 3) when the interface between core and shell is hard to distinguish because they contain the same metal (e.g. small CoFeO_x@Co-MOF, MOF-801@UiO-66).^[22, 70] In other words, when the core nano-objects are ultrasmall or have similar lattice parameters and/or composition than the shell, the conventional characterization methods (SEM, TEM...) are not providing sufficient information about the interface between core and shell matrix, which drive the properties of the core-shell compound. The development of advanced characterization techniques is therefore needed in order to have a better understanding of the properties of the solids and will be presented in this section of the review.^[71]

HRTEM (High-resolution TEM): HRTEM is a key technique to determine the structural and spatial properties of core and shell, such as size/thickness of core and shell, lattice constants, atomic variations, chemical environment... Recently, STEM (Scanning transmission electron microscopy) has been intensively used for its ultra-high resolution (down to sub-50 pm resolutions for aberration correction STEM). It can provide high-quality incoherent images using high-angle scattered electrons in both dark and bright-field modes because of the different Z value of atoms in the core NPs compared with the metal atom of the shell MOF. Therefore, it is usually easy to get meaningful images when the encapsulated NPs are relatively big or containing heavier atoms than the shell. Researchers were able to use aberration-corrected STEM to observe ultra-small nanoparticles (or nanoclusters, size ≤ 2 nm) encapsulated in MOF shell, particularly when the shell is thick.^[69] Energy-dispersive X-ray spectroscopy (called EDS or EDX, usually coupled with TEM/ SEM) is a complementary technique that enables an element distribution mapping within core-shell particles, particularly when the core and shell cannot be easily distinguished from bright/ dark field images,^[68] giving access to information on the loading quantity and distribution of each element. For example, Rogach et al. were not able to identify Cu Nanoclusters (less than 2nm) within the framework of ZIF-8 using conventional STEM image (Figure 8A (a-b)), while EDX mapping (Figure 8A (c-f)) allowed to locate N, Cu and Zn respectively. The uniform loading of Cu evidences the incorporation and homogeneous distribution of Cu NCs through the entire ZIF-8 structure.^[72] In another example, Rosi et al. confirmed a series of multivariate stratified MOF@MOF structure using EDX.^[61] In their case, the core-shell UiO-67(Hf)@UiO-67(Zr) was characterized by EDX line-scan data across single MOF particles that clearly showed the formation of a binary domain stratified MOF with a core-shell structure (Figure 8B). The co-existence of two domains was further confirmed by EDX mapping, where Hf was detected in the entire area of a particle while Zr was only detected in the center. For both STEM and EDS techniques, it should be mentioned that the highly energetic electron beam can damage the MOF structure, as already observed with more robust zeolites, which limits the imaging under typical working conditions. Thus, a careful control the beam intensity as well as the exposure time is required.

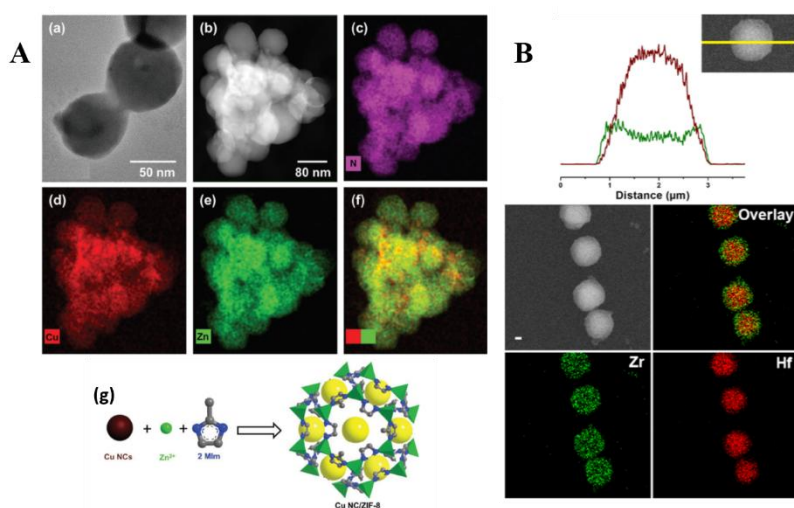


Figure 8. A) (a-b) HRTEM and HAADF-STEM images of Cu NC/ ZIF-8, (c-f) EDS elemental mapping of N, Cu, Zn, and Cu/ Zn, (g) Schematic diagram of the synthesis of Cu NC/ ZIF-8 composites. B) SEM-EDS characterization of stratified UiO-67(Hf)@UiO-67(Zr). Reproduced with permission.^[61, 72] Copyright 2017, Wiley-VCH. Copyright 2019, American Chemical Society.

Other techniques: To determine with a high degree of accuracy the structure of complex core-shell composites, other techniques are usually required. TEM Tomography was rarely used so far regardless of its ability to confirm the 3D architecture probably due to the low stability of MOFs during the long beam exposure time required. Even though, Yang et al. reported recently the utilization of 3D tomography to localize encased Pt-Ni nanoparticles, leading to a reconstructed 3D morphology evidencing that Pt-Ni NPs are located inside ZIF-8 crystals in all three orthogonal slices (Figure 2A (e)).^[43] In addition, indirect characterization techniques can be used in order to verify the respective positions of core and shell. For instance, one of the main features of core-shell NPs@MOF is that active nanoparticles do not occupy the pore space of MOF, and thus do not affect too much its porosity as well as its pore size. To verify this, one typically uses N₂ adsorption porosimetry and checks the total sorption capacity and pore size distribution. However, this method is sometimes not relevant when the loading content is low and cannot be applicable when the NPs are deposited on the MOF surface or when dealing with MOF@MOF core-shells. In the case of the EGS method, the fabrication of the second layer of MOF on the surface of core MOF can lead to an expansion of the crystalline domain size. Therefore, SEM measurements together with the particle size estimation based on the PXRD Bragg peaks width might be combined to get information on the core-shell structure.

4. Core-shell composites for catalysis

Incorporating active “core objects” into a MOF shell is of particular interest for catalysis, due to the broad scope of available encapsulated species, including single and multiple components. It could sometimes lead to a synergistic catalytic effect due to the interaction between active compounds and inorganic nodes/organic ligand of the MOF.^[35, 58, 73, 74] Moreover, the tailorable/ functionalizable porosity of MOF endows the designed composites with tunable sorption selectivity and stability, which are key factors for catalysis.^[59, 75, 76] In

the following section, we will discuss the advances of core-shell MOF-based composites in selective, efficient energy-related catalytic reactions.

4.1 Core-shell Inorganic Nanoparticles (NPs)@MOFs for energy-related applications

4.1.1 CO₂ reduction

The heavy reliance on fossil fuels has led to a significant rise in atmospheric CO₂, which is generally considered as the culprit for global climate change.^[77] The conversion of CO₂ to valuable products, such as CO, CH₄, C₁ or C₂ oxygenated compounds is extremely attractive, but scientifically highly challenging due to the strength of the C=O double bond (806 kJ/mol), which is significantly higher than C-C (336 kJ/mol), C-H (411 kJ/mol), or C-O (327 kJ/mol) bonds.^[78] Accordingly, the catalytic reactivity of core-shell NPs@MOF towards CO₂ reduction was explored due to the possible synergistic effect between metal NPs with the pore functionality of the MOF.

Xu et al reported a series of multi-layered noble metal/ alloy nanoparticles encapsulated in Zn/ Co based-MOFs for CO₂ reduction.^[79, 80] As shown in Figure 9(A), monodispersed core-shell Au@Pd bimetallic nanoparticles (size=17 nm) were successfully incorporated in the center of a Co-MOF and Pt NPs were subsequently loaded on the outer surface of Au@Pd@1Co architecture to build Pt/Au@Pd@1Co composites (Figure 9(B-C)). The CO₂ reduction tests in Figure 9(D) suggested that 8-Pt/Au@Pd@1Co (4, 8, or 12 represent the volume of the Pt NPs solution) owned the best conversion among all the analogs due to their relatively high Pt NPs content, and an excellent selectivity in comparison with Au@Pd@1Co and 4-Pt/1Co. These results (Figure 9(F)) revealed that the loaded Pt NPs enhanced the conversion of CO₂, while Au@Pd NPs dramatically changed the proportion of CO to CH₄ in the products. The authors also found that the temperature had a positive impact on the CO₂ conversion and CO selectivity. When increasing the temperature from 300 to 400 °C (Fig 9(E)), the conversion of 4-Pt/Au@Pd@1Co increased from 4.38% to 15.6%, and the CO selectivity increased from 73.4% to 87.5%. This may be attributed to the opposite processes of CO generation (endothermic) and CH₄ generation (exothermic). The mechanism for the formation of CO was attributed to the redox properties of active metal centers ($\text{CO}_2 + \text{M}^{n+} \rightarrow \text{MO}_x + \text{CO}$, $\text{H}_2 + \text{MO}_x \rightarrow \text{M}^{n+} + \text{H}_2\text{O}$), while the MOF enabled an enhanced adsorption of CO₂ molecules near the catalyst. The bimetallic Au@Pd are indeed active for C=O bond hydrogenation and decomposition of oxygenated molecules while Pt NPs serves as additional active sites for conversion due to the limited pore volume of MOF and low content of Au@Pd. In contrast, the formate decomposition mechanism for the reverse Water-Gas Shift Reaction (WGSR indicates the reaction of carbon monoxide and water vapor to form carbon dioxide and hydrogen) is unlikely to occur due to the narrow pores of the host MOF, which may also contribute for the high selectivity towards CO production (tetrahedron CH₄ is larger than linear CO).^[80]

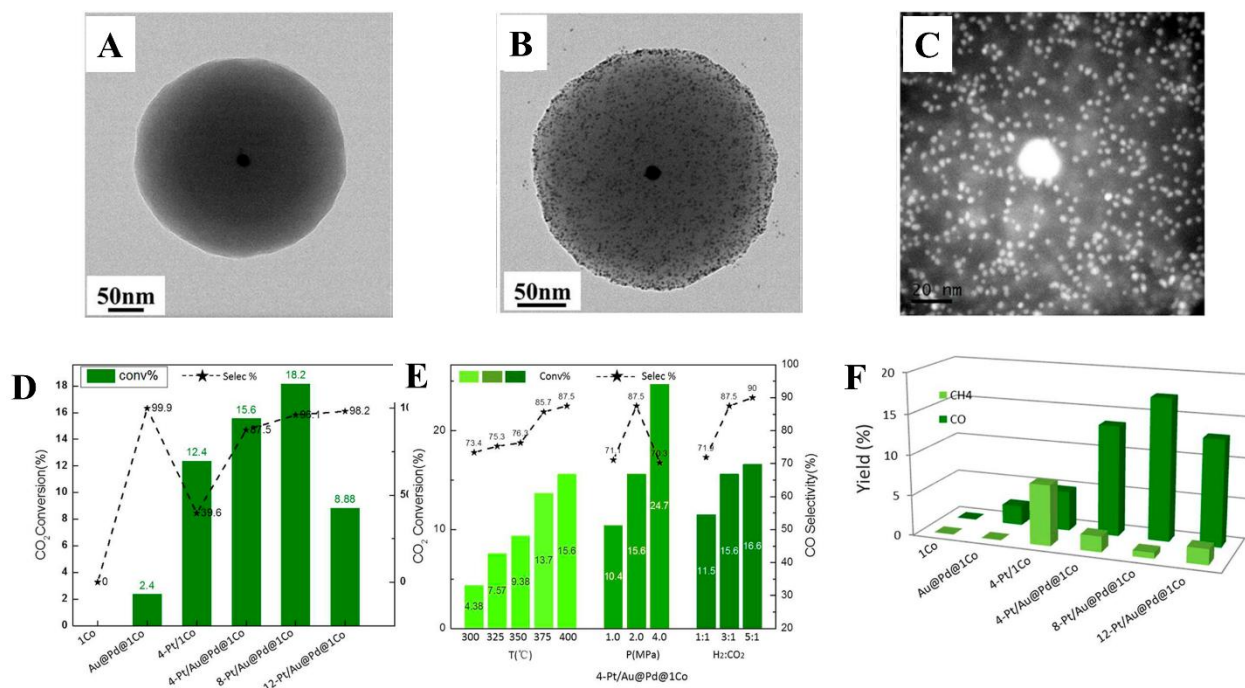


Figure 9. A) HRTEM images of Au@Pd@1Co. B) HRTEM images of Pt/Au@Pd@1Co. C) HADDF-STEM image of the detail of Pt/Au@Pd@1Co particle. D) CO₂ conversion and CO selectivity of the different catalysts for RWGS (reverse water-gas shift). E) CO₂ conversion and CO selectivity at different reaction conditions for RWGS. F) Yield of the different catalysts for RWGS. Reproduced with permission.^[80] Copyright 2018, ACS.

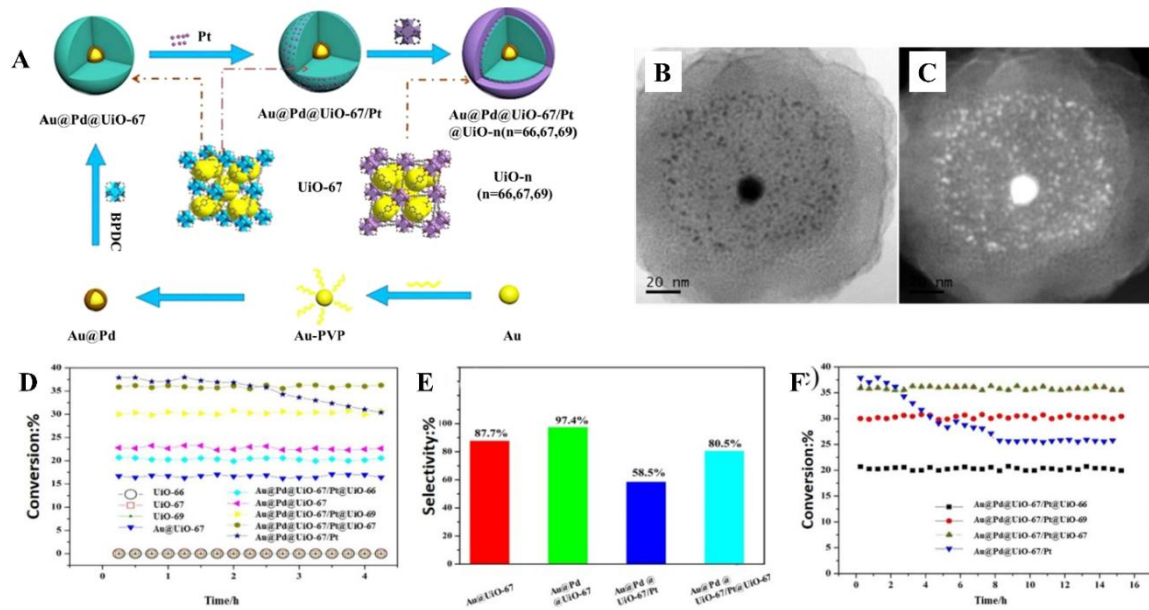


Figure 10. A) Synthetic route for sandwich Au@Pd@UiO-67/Pt@UiO-*n* and their nanocomposites. B-C) HAADF-STEM images of Au@Pd@UiO-67/Pt@UiO-67. CO₂ conversion and CO selectivity D) CO₂ conversion for the catalysts at 400 °C, E) CO selectivity for the catalysts at 400 °C, F) stability for the catalysts at 400 °C by a longevity test. Reproduced with permission.^[81] Copyright 2019, ACS.

Similarly, the authors recently reported other spherical sandwich core-shell structures Au@Pd@UiO-67/Pt@UiO-*n* (*n*=66, 67, 69) for efficient CO₂ conversion. The synthetic

schematic diagram for the sandwich core-shell structure is shown in Figure 10(A). The monodispersed Au@Pd alloy and well-localized Pt NPs were characterized by STEM (Figure 10(B-C)). The size of the encased Au@Pd NPs was 16.6 nm and the one of Pt NPs of 3.3 nm. The catalytic results in Figure 10(D-E) demonstrated that 1) even though Au@Pd@UiO-67/Pt (Pt on the surface of Au@Pd@UiO-67) exhibited an increased conversion, the selectivity for CO decreased due to the further hydrogenating of CO to form CH₄; 2) Au@Pd@UiO-67/Pt@UiO-66 showed the lowest conversion efficiency but highest selectivity in Au@Pd@UiO-67/Pt@UiO-*n* (*n* = 66, 67, 69), highlighting the impact of the porosity of the outer shell on the conversion and selectivity; 3) the thicker the outer shell is, the higher selectivity but a lower conversion was observed because the shell thickness slowed down the reactant and product diffusion. As seen in Figure 10(F), long-term catalytic tests suggested the superior stability of Au@Pd@UiO-67/Pt@UiO-*n* (*n* = 66, 67, 69) compared to Au@Pd@UiO-67/Pt due to the lack of outer MOF preventing the Pt NPs from migration and agglomeration in the second compound.^[81]

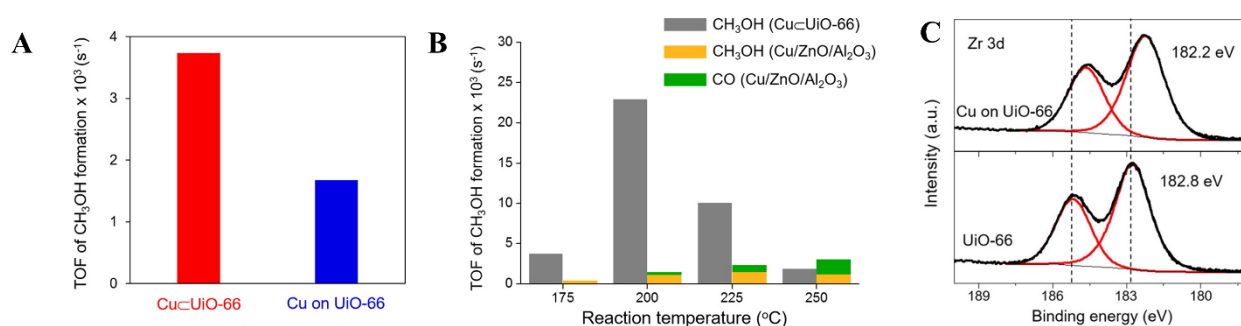


Figure 11. A) Initial turnover frequency (TOF) of methanol formation over Cu@UiO-66 and Cu on UiO-66. B) TOFs of product formation over Cu@UiO-66 catalyst and Cu/ZnO/Al₂O₃ catalyst at various reaction temperatures. C) XPS Zr 3d spectra of UiO-66 and Cu on UiO-66. Reproduced with permission.^[35] Copyright 2016, ACS.

Apart from the use of noble metal nanoparticles as active centers, non-noble nanoparticles driving CO₂ reduction catalysts are of strong interest due to their much lower cost and higher availability. Notably, Cu-based catalysts showed remarkable reactivity.^[82] Yaghi et al. synthesized 18 nm Cu nanocrystals encapsulated within or outside UiO-66 particles to give Cu@UiO-66 (core-shell structure) or Cu on UiO-66, (Figure 1B)), with 1 and 1.4 % of loaded according to ICP-AES analysis, respectively. A series of benchmark supports (UiO-66, MIL-101(Cr), ZIF-8, mesoporous silica MCF-26, ZrO₂, Al₂O₃) were also selected to encapsulate Cu. However, when performing catalytic evaluation (T=175°C, gas flow of CO₂/H₂ (1/3) at 10 bar), neither Cu@MIL-101(Cr) nor Cu@ZIF-8 showed reactivity towards methanol unlike the Zr-O and Zn-O based supports. By comparing the reactivity between Cu@UiO-66 and Cu on UiO-66, the authors found that the location of the Cu nanocrystals did not affect the catalytic activity (Figure 11(A)). Cu@UiO-66 showed however more than a 2-fold improved TOF value ($3.7 \times 10^{-3} \text{ s}^{-1}$ versus $1.7 \times 10^{-3} \text{ s}^{-1}$) and an enhanced stability in working conditions. The authors assumed that the higher number of contact points between Zr₆ oxo-clusters and the surface of the Cu NPs did lead to an increase of the reactivity. Notably, Figure 11(B) showed that despite the increased content of CO when elevating the temperature in the benchmark Cu/ZnO and Zn/Al₂O₃, no CO was generated in the Cu@UiO-66 catalyst whatever the temperature. The high selectivity is associated to the fact that the reverse water-gas shift reaction is endothermic, which means the CO product is favored at a higher

temperature. XPS analysis was performed to shed light on the high selectivity of Cu on UiO-66. The Zr 3d spectrum of catalyst (Fig. 11(C)), particularly the Zr 3d_{5/2} peak shift from 182.8 to 182.2 eV in comparison with pristine UiO-66, indicated that the Zr(IV) is reduced when in close interaction with Cu nanocrystals. This finding will hopefully promote the discovery of other more efficient and cheap Cu@MOFs catalysts.^[35]

Selective CO₂ reduction reaction has so far been tentatively explored via the use of core-shell composites. Nevertheless, from a practical application point of view, strong efforts are still required to develop more efficient core-shell catalysts in CO₂ reduction particularly through the use of cheaper core and shell materials. One can imagine enhancing the efficiency by either optimizing the host-guest interactions or the relative ratio of incorporated active sites, or by decreasing the size of the active nanoparticles, while a better understanding of the impact of the interaction between the MOF and the Cu nanoparticles is needed.

4.1.2 H₂ Production

H₂ is considered as the most promising new generation sustainable fuel due to the escalating depletion of traditional fossil fuel resources and the growing threat of environmental pollution. Series of emerging heterogeneous catalysts started to draw scientists' attention in recent years. However, the generation of H₂ from H₂O still faces massive challenges and MOFs-based composites (with active NPs) showed interesting properties for this reaction due to their possible combination with a large amount of guest active materials.

Nie et al. followed a template-sacrificing synthesis strategy to encapsulate a series of noble-metal sensitized semiconductors (ZnO@M, M= Au, Pt, Ag) in ZIF-67 for photoelectrochemical (PEC) water splitting.^[83] Since ZnO@Au@ZIF-67 showed remarkably improved photoconversion efficiency and photocurrent density, this example is discussed in detail. As displayed in Figure 12(A-B), a core-shell structure with 85 nm core and 18 nm shell was prepared. The catalyst was applied as photo-anode for PEC water splitting under UV-visible spectrum illumination. The current intensity of ZnO@Au@ZIF-67 was largely boosted (to 1.93 mA.cm⁻²) by using Au NPs in comparison with the pure ZnO (0.38 mA.cm⁻²), which can be attributed to the enhanced visible-light absorption offered by the Au SPR (Surface Plasmon Resonance) effect (Figure 12(C)). Subsequently, both the O₂-evolution rate and the photocurrent were monitored simultaneously to evaluate the efficiencies and stabilities of PEC water splitting. As shown in Figure 12(E), the ZnO@Au@ZIF-67 showed the highest average O₂-evolution rate among all catalysts (ZnO@ZIF-67, ZnO@Au@ZIF-8, ZnO@Au, and ZnO), which was 4.9 times higher than the one of ZnO. Notably, the PXRD patterns and SEM images confirmed the excellent stability of ZnO@Au@ZIF-67 in PEC water splitting after several catalytic cycles. As a proof-of-concept, the strategy was extended to other active nanoparticles, including Ag, Pt and both of them showed comparable reactivity towards water splitting. Even though the moderate catalytic efficiency is still far from real application in comparison to benchmarks (e.g., BiVO₄, perovskite), it can nevertheless give useful indications to further improve the overall efficiency of such composites.

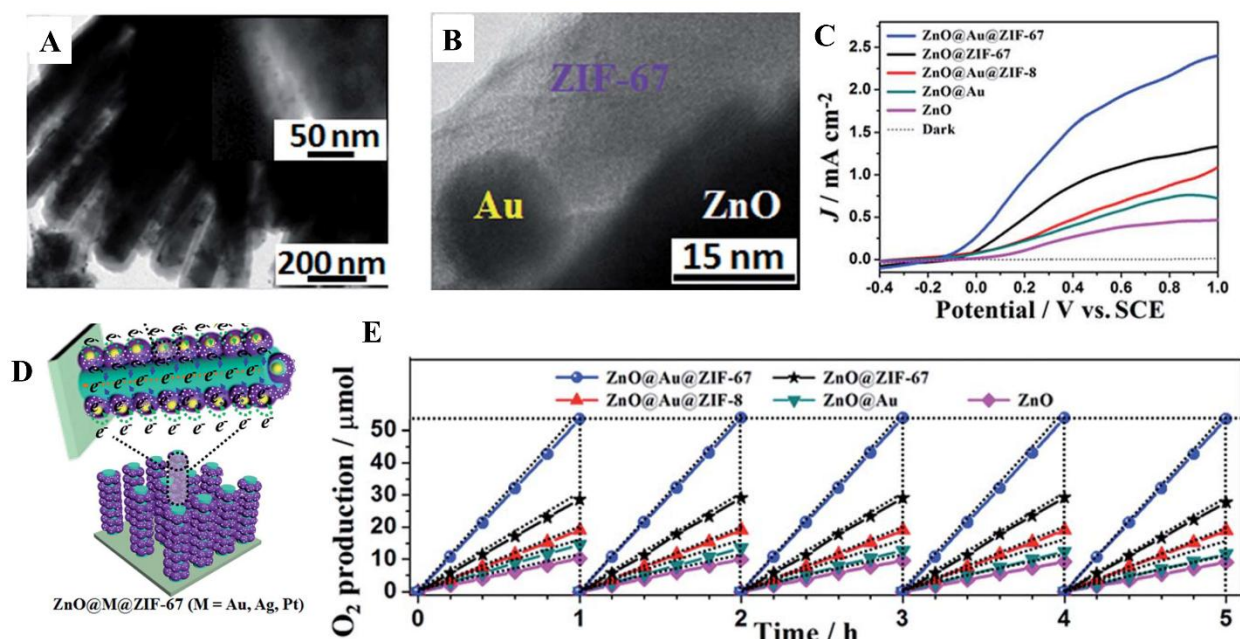


Figure 12. A) TEM image of ZnO@Au@ZIF-67. B) HRTEM image of ZnO@Au@ZIF-67. C) J - V curves for several compounds. D) Schematic illustration of the fabrication of the ZnO@M@ZIF-67 photo-anode for PEC water splitting. E) O₂-production performance under full-spectrum illumination ($\lambda > 200$ nm) over five cycles on ZnO@Au@ZIF-67. Reproduced with permission.^[83] Copyright 2017, Royal Society of Chemistry.

The water-gas shift (WGS) reaction ($\text{H}_2\text{O} + \text{CO} \rightarrow \text{H}_2 + \text{CO}_2$) is a promising way to produce H₂ that is however rate-limited by the activation of H₂O.^[84] To address this, Kitagawa et al. proposed the use of highly hydrophilic UiO-66 as support for Pt Nanocrystals (Pt NCs) with distinct spatial distribution, that is, Pt NCs on the surface of UiO-66 (Pt on UiO-66) and core-shell structure (Pt@UiO-66) (Figure 13(A-B)). The H₂O sorption isotherms (Figure 13C) confirmed the maintained porosity of the composites. As shown in Figure 13(D), the conversion of CO into CO₂ increased with temperature for both the composites and Pt deposited on ZrO₂. The Pt@UiO-66 owned the highest conversion at 340°C (10.8%), compared with that of Pt on UiO-66 (8.1%) and of Pt on ZrO₂ (6.4%). *In-situ* Infrared-mass spectra (IR-MS) measurements demonstrated that Pt@UiO-66 owns a better H₂O adsorption, therefore enhancing the formation of Pt-OH bonds compared to Pt on UiO-66 and Pt on ZrO₂. As additional evidence, when the thickness of the MOF shell decreased from 80 to 40 nm, the reactivity of Pt@UiO-66 exhibited higher WGS reaction activity than both Pt@UiO-66-80nm and Pt on UiO-66 (Figure 13(F)). Furthermore, after 5 cycles, the catalytic activity of Pt@UiO-66-40nm did not change, confirming the high stability of Pt@UiO-66-40nm.^[73] This example clearly revealed that hydrophilicity, tight host-guest interaction, as well as shell thickness all affect the reactivity of MOF-based core-shell WGS catalysts, which give insights for the development of catalysts with higher activity.

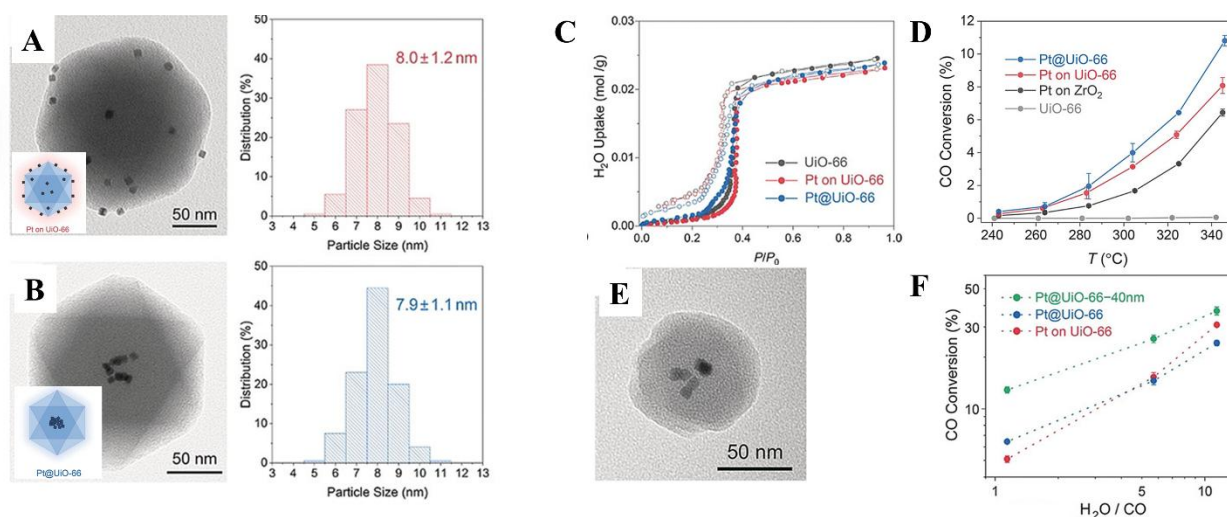


Figure 13. TEM images and particle size distribution (insert: schematic images) of A) Pt on UiO-66 and B) Pt@UiO-66. C) H₂O adsorption isotherms at 298K with adsorption represented by closed circles and desorption by open circles. (P/P_0 : relative pressure). D) Temperature dependence of CO conversion on WGS reaction. The flow rate was H₂O/ CO/ Ar = 11/ 10/ 50 sccm (standard cubic centimeters per minute), and the pressure was 0.65 MPa. E) TEM images of Pt@UiO-66-40nm. F) a) CO conversion versus H₂O/CO ratio for WGS reaction over Pt on UiO-66 (red), Pt@UiO-66 (blue), and Pt@UiO-66-40nm (green). Reaction conditions: 11.4, 57.0, or 114 sccm of H₂O, 10 sccm of CO, 50 sccm of Ar, 0.65 MPa and 320 °C. Reproduced with permission.^[73] Copyright 2019, Wiley-VCH.

Subsequently, the same group studied the influence of ligand functionalization on the H₂O activation. As illustrated in Figure 14 (A-D), the Pt NCs were encapsulated in several functionalized UiO-66 frameworks. The ligand functionalization significantly affected the catalytic activity of the WGS reaction (Pt@UiO-66-Me₂ > Pt@UiO-66-H > Pt@UiO-66-Br) (Figure 14 (E)). These differences in reactivity were attributed to the different chemical states of H₂O in UiO-66 as -Br functional groups could provide relatively hydrophilic pores with a higher affinity to H₂O while -Me₂ functional groups could lead to more hydrophobic pores with a lower affinity to H₂O. The chemical shifts of the adsorbed H₂O obtained by ¹H NMR (Figure 14(F) revealed that the adsorbed H₂O and Zr-OH are relatively mobile and exchangeable (3.5, 3.8, and 3.3 ppm for Pt@UiO-66-H, Pt@UiO-66-Br, and Pt@UiO-66-Me₂, respectively), while the signals from aromatic rings are not affected by water sorption. The highest H₂O chemical shift observed for Pt@UiO-66-Br indicates a decrease in electron density of proton compared to pristine Pt@UiO-66-H. Moreover, *In-situ* IR was applied to confirm the formation of OH species resulting from H₂O activation (Figure 14G). With Pt@UiO-66-Me₂, intense IR bands at 3734-3765 cm⁻¹ and 3533 cm⁻¹ could be attributed to the Pt-OH and Pt-COOH bands, the former one being an active intermediate in WGS reaction and the latter one corresponding to an intermediate species formed from Pt-CO and Pt-OH. This revealed that apart from the core-shell encapsulation, the direct MOF functionalization is a convenient strategy to improve the catalytic properties.^[75]

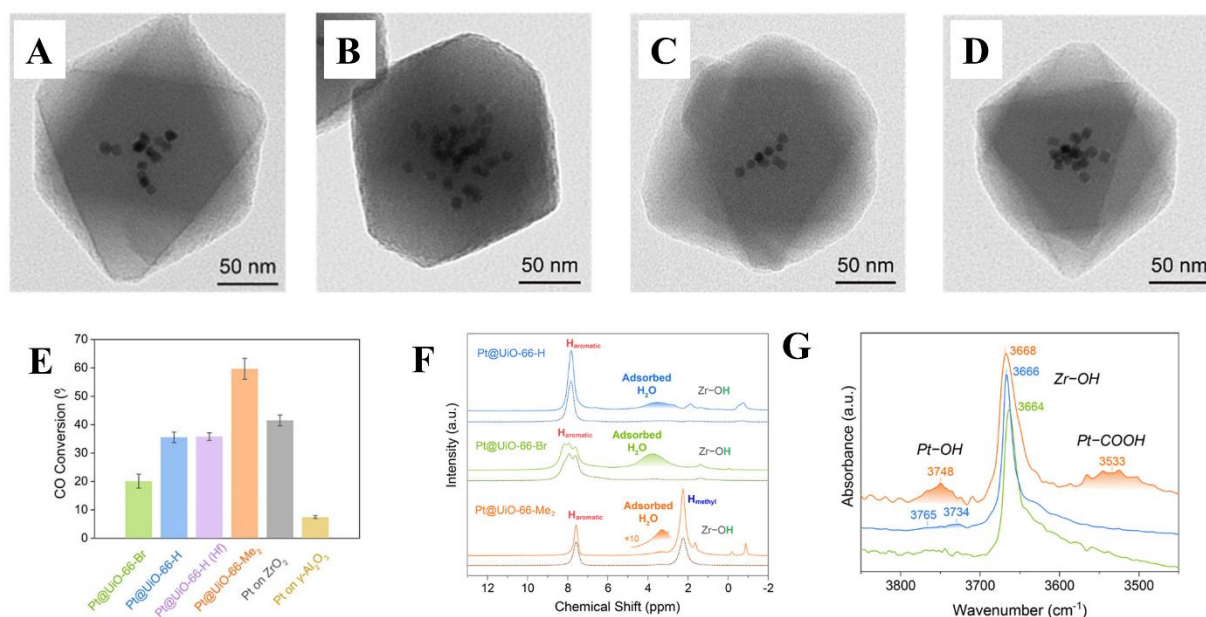


Figure 14. A) Pt@UiO-66-H. B) Pt@UiO-66-H(Hf). C) Pt@UiO-66-Br. and D) Pt@UiO-66-Me₂ nanoparticles observed by TEM; E) CO conversion in the WGS reaction at 340 °C. Reaction conditions: 114 sccm of H₂O, 10 sccm of CO, 50 sccm of Ar, and 0.65 MPa. F) ¹H ultrafast (70 kHz) MAS NMR spectra (top, solid lines) and the corresponding ¹H DQNMNMR spectra (bottom, dashed lines) of Pt@UiO-66 analogues at room temperature, where the peaks attributed to adsorbed H₂O are highlighted. The unlabeled peak around 6.5 ppm corresponds to the residual ligand. G) *In situ* IR spectra during WGS reaction at 300 °C for Pt@UiO-66-H (blue), Pt@UiO-66-Br (green), and Pt@UiO-66-Me₂ (orange) under a mixed gas flow (H₂O/CO/N₂ = 4.5/0.4/15.1 sccm). Reproduced with permission.^[75] Copyright 2019, ACS.

With the incorporated active nanoparticles and the photo-responsive components of the MOF, the NPs@MOFs often show an enhanced UV and even visible light absorption, making them promising for photocatalytic H₂ generation. The highly designable pore/channel space provides a wide range of possibilities in order to tune the transport distance of charge carriers to the MOF, which therefore may effectively suppress the fast recombination of electron-hole pairs that is one of the main parameters limiting the photocatalytic efficiency of semiconductors.^[85] For example, Jiang et al. reported that ca. 3nm Pt nanoparticles could be encapsulated inside (Pt@UiO-66-NH₂) or supported (Pt/UiO-66-NH₂) on UiO-66-NH₂ (Figure 15 (A-D)). Interestingly, the difference in the NPs spatial position led to a distinct catalytic reactivity. As displayed in Figure 15 (E-F), compared to the poor hydrogen production efficiency (1.72 μmol.g⁻¹.h⁻¹) of pristine UiO-66-NH₂, the Pt/UiO-66-NH₂ and Pt@UiO-66-NH₂ showed around 30 times (50.26 μmol.g⁻¹.h⁻¹) and 150 times (257.38 μmol.g⁻¹.h⁻¹) higher reactivity, respectively, suggesting that the charge separation between MOF and Pt plays an important role in catalytic efficiency. These results evidenced that, all other parameters being fixed, the NPs incorporated in UiO-66-NH₂ present a higher photo-catalytic efficiency than the one located at the MOF surface, probably due to the shorter distance between Pt NPs and the host MOF. In this study, the authors applied ultrafast transient absorption (TA) spectroscopy and transient luminescence spectroscopy to analyze the photo-excited carrier dynamics of nanocomposites systems (Figure 15G-H). The mean excited state and PL lifetimes (Figure 15H-I) decrease from UiO-66-NH₂ to Pt/UiO-66-NH₂, and Pt@UiO-66-NH₂, respectively, which can be attributed to the opening of an additional electron transfer channel from UiO-66-NH₂ to Pt NPs in Pt@UiO-66-NH₂ due to the shortened electron-transport distance, in line with a suppression of the photo-excited charge recombination in these materials.^[74]

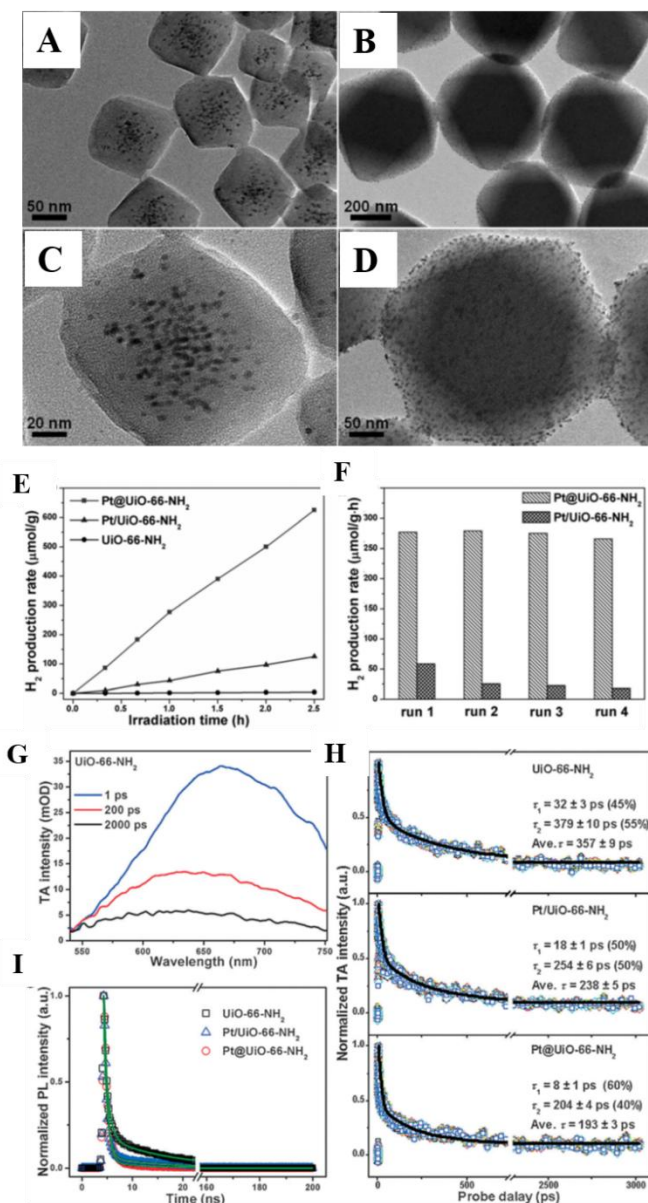


Figure 15. Typical TEM images of A), C) Pt@UiO-66-NH₂ and B), D) Pt/UiO-66-NH₂. E) Photocatalytic hydrogen-production rates of UiO-66-NH₂, Pt@UiO-66-NH₂ and Pt/UiO-66-NH₂. F) Recycling performance comparison between Pt@UiO-66-NH₂ and Pt/UiO-66-NH₂. G) TA spectra of UiO-66-NH₂ with TA signal given in mOD (OD: optical density). H) TA kinetics, and I) Time-resolved PL decay profiles for UiO-66-NH₂, Pt@UiO-66-NH₂, and Pt/UiO-66-NH₂, respectively ($\lambda_{\text{ex}}=400$ nm, $\lambda_{\text{em}}=455$ nm). Reproduced with permission.^[74] Copyright 2016, Wiley-VCH.

Other studies demonstrated that the preparation of core-shell structures could provide unprecedented chemical designability, unexpected catalytic reactivity, and open up more opportunities for energy-related applications.^[35, 73] It is doubtless that this domain will continue to draw intensive attention in a near future, particularly to design more efficient non-noble metal containing MOF catalysts with better photophysical properties, durability, visible light absorption with the ultimate ambition to develop efficient noble metal free overall water splitting photocatalysts.

4.2 Core-shell Nanoparticles (NPs)@ MOFs structures for organic synthesis

MOFs comprising several types of active sites are of interest as multifunctional heterogeneous organic catalysts. Incorporating additional active species in MOF could not only endow a synergistic effect but also give rise to unprecedented high selectivity due to the contribution of the well-defined pore size and chemical nature of the MOF. Thus, in this section, we summarize the recent progresses in heterogeneous organic catalysis relying on core-shell MOF based composites.

The selective hydrogenation of the carbon-oxygen group from α , β -unsaturated alcohols is a widely studied but highly challenging catalytic reaction due to the thermodynamically favored carbon-carbon hydrogenation. Therefore, the selectivity/ conversion/ reusability obtained using pure noble metal Nanoparticles based catalysts (e.g., Pt NPs,^[86] Au NPs^[87]). To this end, Tang et al. showed that MOFs coupled with Pt NPs forming sandwich structures can be effective selectivity regulators for the hydrogenation of α , β -unsaturated aldehydes. The heterogeneous catalysts were developed by epitaxial growth of a mesoporous MIL-101(Cr, Fe) shell on the Pt NPs@MIL-101(Cr) core (Figure 16(A)). The shell thickness and the nature of the metal nodes were optimized and the compound MIL-101(Cr)@Pt@MIL-101(Fe)^{2,9} (2.9 refers to the shell thickness expressed in nm) was finally selected. Figure 16(B) shows the well-defined Pt NPs spatial distribution as well as the highly ordered structure of the compound, which presents an excellent selectivity along with almost full conversion for the transformation of cinnamaldehyde to cinnyl alcohol (Figure 16(E)). The reusability tests evidenced the unaltered high conversion, high selectivity and also maintained crystallinity during five successive catalytic cycles (Figure 16(C, D)). Density functional theory calculations indicated that the preferential interaction of the C=O bond of cinnamaldehyde with the Coordinatively Unsaturated Sites (CUS) of the MOF was thermodynamically favored and that at the same time, the formation of cinnyl alcohol was more energetically favored than other byproducts.^[58] This example evidences that high activity can be obtained using MOF-based core-shell particles. However, attention should be paid in developing highly selective catalysts using less expensive and/or toxic active centers.

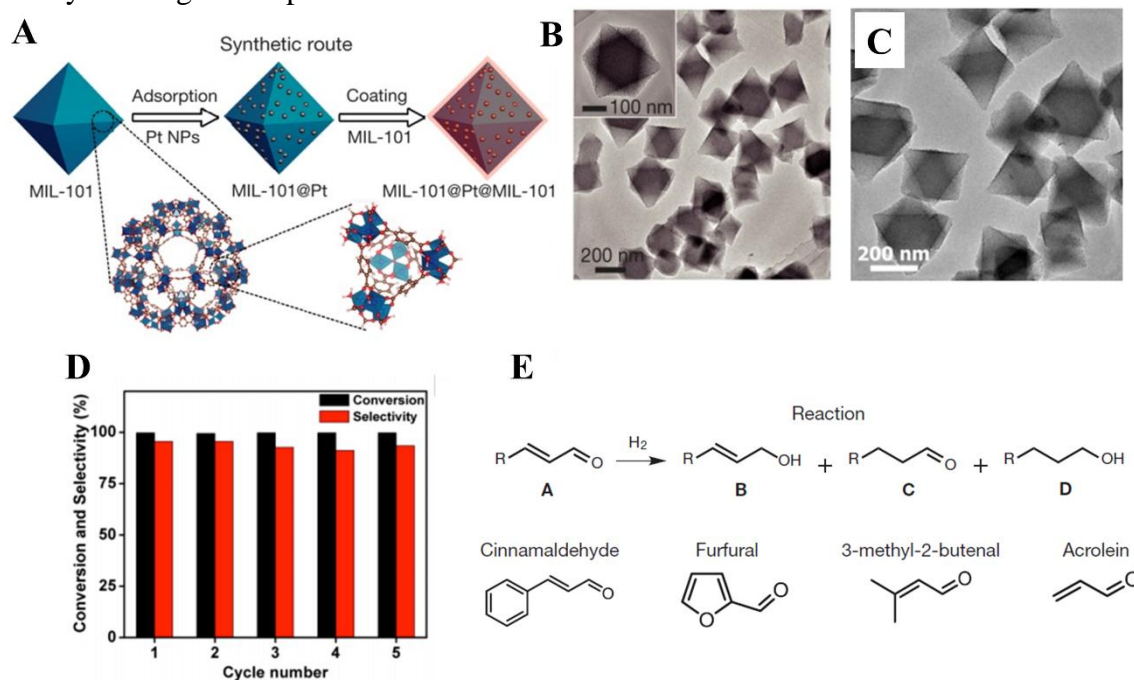


Figure 16. A) Illustration of the synthetic route to generate MIL-101@Pt@MIL-101, comprising Pt nanoparticles (NPs) sandwiched between a core and a shell of MIL-101. B) TEM image of MIL-101(Cr)@Pt@MIL-101(Fe)^{2,9} C) TEM image of MIL-

101(Cr)@Pt@MIL-101(Fe)^{2,9} after cycling catalytic tests. D) Stability tests of MIL-101(Cr)@Pt@MIL-101(Fe)^{2,9} for hydrogenation of cinnamaldehyde to cinnyl alcohol. E) Schematic diagram of hydrogenation of α , β -unsaturated aldehydes. Reproduced with permission.^[58] Copyright 2016, Nature Publishing Group.

In another example, Huang et al. *in-situ* grew MOF-74 on preformed uniform bimetallic Pt-Ni nanowires (NWs) using the MOF's ligands to capture the dissolved Ni²⁺ during the dealloying process. TEM images and EDS mapping in Figure 17(A-B) evidenced that the Pt-Ni NWs were well encapsulated in a MOF-74 shell. The shell thickness could be readily adjusted by tuning the amount of Ni from the initial Pt-Ni NWs as well as the amount of introduced reactants during the MOF growth (Figure 17(C-D)). The hydrogenation of cinnamaldehyde (CAL) (Figure 17(E)) was used to investigate the reactivity and conversions close to 100% were reported for Pt-Ni_(1.6, 2.09, 2.20) NWs@Ni/Fe_x-MOF ($x=2, 3, 4, 5$ mg, corresponding to the mass of introduced FeCl₃·6H₂O) with different Ni and Fe contents.^[88]

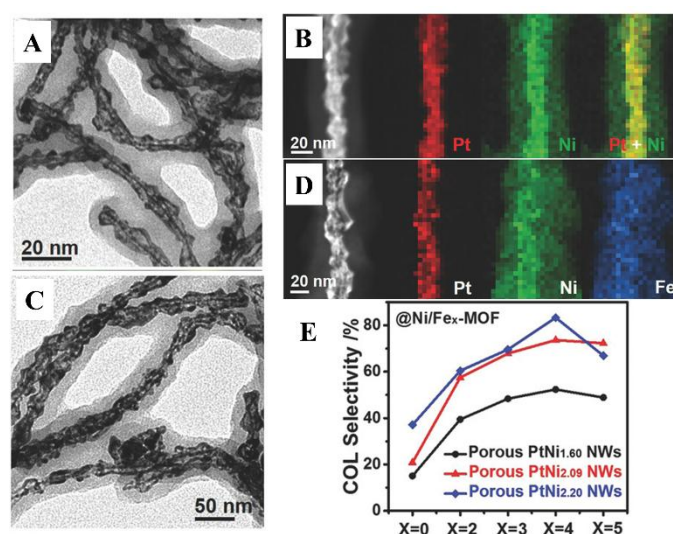


Figure 17. A) TEM image of PtNi_{2.20} NWs@Ni-MOF. B) HAADF-STEM image and EDS mappings of PtNi_{2.20} NWs@Ni-MOF. C) TEM image of PtNi_{2.20} NWs@Ni/Fe₄-MOF. D) HAADF-STEM image and EDS mappings of PtNi_{2.20} NWs@Ni/Fe₄-MOF. E) Catalytic performance of the different catalysts. Reproduced with permission.^[88] Copyright 2018, Wiley-VCH.

Similarly, MOF can serve as support not only to prevent active nanoparticles from aggregation but also to contribute to the enhancement of the selectivity and/or conversion for several organic reactions. Other recent progresses are listed in Table 2.

Even though the combination of active NPs and MOFs can be achieved using alternative methods such as impregnation, deposition-precipitation, surface grafting or chemical vapor deposition, these techniques can lead to leaching or aggregation of active NPs during the course of the heterogeneous catalytic reaction. Core-shell structures can solve this issue by embedding the NPs within the MOF particles. Apart from the confinement of active particles in core-shell composites, remarkable synergetic effects led to promising catalytic performances (e.g., Ref 29, 66, 67, 53) such as enhancement of the selectivity and/or conversion. Indeed, the *in-situ* growth of shell on the surface of the core objects allows a close packing between NPs and MOFs, which enables efficient energy/charge transfer between the

MOF and the active NPs, similar to Schottky junctions observed in the metal-semiconductor materials.^[89] This synergetic effect has been widely observed in both gas and liquid based catalysis (see Table 1). Very recently, the strengthening of the interaction between active NPs and MOFs has been alternatively achieved by partial deligandation of metal/ MOF composites.^[90] This controlled deligandation of the MOF induces much more accessible Cr-O metal sites while maintaining the MOF porosity. This enables a stronger interaction with the guest active NPs, achieving similar synergetic effects than in core-shell composites. This example evidenced that the strong interaction between NPs and MOFs is one of the key to explain the overall catalytic performance, even though the authors prepared such composites by loading metal NPs in the pores of MOFs.

Table 2. Summary of the catalytic applications based on core-shell composites.

Core	Shell	Shell role	Synthesis method	Core size (nm)	Shell thickness (nm)	Content (wt %)	Applications	Refs
Pd NPs	UiO-66/ 67/ 68	Synergy*	EGS	3.5	35-50	0.59-0.66	Semihydrogenation	[59]
Pd NPs	UiO-66(Hf)	Synergy	CAAS	7.6	NA	5.2	Hydrogenation	[91]
Fe ₃ O ₄	Cu ₃ (BTC) ₂	Synergy	CAAS	230	60	NA	Aerobic oxidation	[92]
Copper hydroxysulfates	HKUST-1	Synergy	TSS	NA	NA	NA	Acetalization	[93]
Au@Pt Nanotubes	ZIFs	Synergy	CAAS	52	250	0.84-2.5	Semihydrogenation	[94]
Pt-Pd NCs	UiO-67	Synergy	CAAS	49-60	120	1.93 Pt 0.055 Pd	Reverse water-gas shift reaction	[95]
Au@Pd NPs	UiO-66	Synergy	CAAS	16-17	98	NA	CO ₂ hydrogenation	[34]

UiO-66	UiO-66-F ₄	Synergy	EGS	50-80	NA	NA	Dye adsorption Sulfide Oxidation	[96]
Pt NPs	UiO-66-NH ₂	Synergy	CAAS	3	NA	2.87	Photocatalytic Hydrogen- production	[74]
Pd NPs	ZIF-8	-	TSS	4.5	NA	1.1	Hydrogenation of olefins	[97]
Au@Pd, Pt NPs	UiO-67	Synergy	CAAS, EGS	16.6 Au@Pd NPs 3.3 Pt NPs	9.1-18.3	0.64 Pt, 0.36 Au, 0.074 Pd	Reverse water-gas shift reaction	[81]
Au@Pd, Pt NPs	1Co	Synergy	CAAS	17 Au@Pd	130	NA	CO ₂ to CO	[80]
Au ₂₅ NCs, ZIF-8	ZIF-67	Synergy	EGS	1.2	2-25	1	Carboxylation of phenylacetylene	[60]
ZnO@Au	ZIF-67	Synergy	CAAS	85	18	1.08	Photoelectrochemic al water splitting	[83]
Pt NPs	UiO-66-NH ₂	Synergy	CAAS	NA	NA	NA	H ₂ generation	[98]
CdS	ZIF-8	Synergy	CAAS	70	13.6-102	NA	Photocatalytic H ₂ generation	[99]

UiO-66	UiO-67-BPY	Synergy	EGS	150	50	NA	Knoevenagel condensation	[100]
ZIF-67	Co-MOF-74	Synergy	TSS	450-490	10-50	NA	Water oxidation reaction	[23]
Au@Pd	MOF-74	Immobilization*	CAAS	14	NA	0.095 Au 0.035 Pd	CO ₂ conversion	[79]
Au@Pd	Co ₂ (oba) ₄ (3-bpdh) ₂	Immobilization	CAAS	17	135	NA	CO ₂ conversion	[80]
PtNiNWs	Ni/Fe ₄ -MOF	Synergy	CAAS	20	NA	NA	Cinnamaldehyde hydrogenation	[88]
Pt NPs	Ni/ Zn-MOF	Immobilization	CAAS	5	NA	0.15	Cinnamaldehyde hydrogenation	[101]
UiO-66	UiO-67-BPY/ Ag	Synergy	EGS	150	50	0.73 Ag	CO ₂ fixation via carboxylation	[102]
Cu@ Pd	ZIF-8	Synergy	CAAS	61	600-1000	5.5 mol% Cu 0.1 mon% Pd	Selective Hydrogenation of different Alkynes	[103]
Fe ₃ O ₄ @PDA-Pd	Cu-BTC	Synergy	CAAS	530	10	2.27 Pd	Reduction of 4-nitrophenol	[104]

Pd NCs	MIL-101(Fe)	Synergy	CAAS	12.3	NA	59.5	Hydrogenation of α , β -unsaturated carbonyl compounds	[25]
Pt NPs	ZIF-8, ZIF-71	Immobilization	CAAS	4.3	NA	3	Hydrogenation of cinnamaldehyde	[105]
Pt-CeO ₂	UiO-66-NH ₂	Synergy	CAAS	50-180	8-30	1 Pt	Hydrogenation of Furfural	[106]
Rh-Ni	MOF-74(Ni)	Synergy	TSS	NA	2-50	NA	Hydrogenation of Alkyne	[107]
Pt NCs	UiO-66-H	Synergy	CAAS	7.9-8.0	NA	6.7	Water-gas shift reaction	[75]
	UiO-66-H(Hf)					4.6		
	UiO-66-Br					5.3		
	UiO-66-Me ₂					5.9		
Ni ₂ P/ Ni ₁₂ P ₅	UiO-66-NH ₂	Synergy	CAAS	10	NA	0.512 0.559	Photocatalytic H ₂ production	[108]
Pt NPs	UiO-66	Immobilization	CAAS	7.9	80	6.7	Water-gas shift reaction	[73]

Cu NCs	UiO-66	Immobilization	CAAS	18	NA	1.4	CO ₂ reduction	[35]
TS-SnO ₂ - HoMSs	MIL- 100(Fe)	Synergy	CAAS	>500	50	97	Lithium Storage	[27]

NA: Not Available

Table 3: Summary of the other applications based on core-shell composites.

Core	Shell	Shell function	Synthesis method	Core size (nm)	Shell thickness (nm)	Content (wt %)	Applications	Refs
Zns QDs	ZIF-67	Immobilization	CAAS	5	NA	NA	Cu ²⁺ detection	[109]
NaYF ₄ : Yb, Er	MIL-101- NH ₂ (Fe)	Immobilization	CAAS	40	NA	NA	Bio-imaging	[110]
Au Nanorod	MIL- 88(Fe)	Immobilization	CAAS	40	NA	NA	Bio-diagnosis	[111]
HKUST-1	MOF-5	Improved adsorption capacity	NA	100	NA	10	CH ₄ storage	[112]
MIL-101- NH ₂ (Al)	ZIF-8	Enrichment	CAAS	NA	NA	15%	Detection and removal of Cu ²⁺	[113]

Au NRs	Zr-Porphyrinic	Immobilization	CAAS	53.8*25.2	8.1-13.2	NA	Photodynamic/ Photothermal/ Chemotherapy of Tumor	[41]
Zn ₃ (BPD C) ₃ (BiPY)	Zn(BPDC)(BPP)	Improving selectivity	TSS	NA	NA	40.1	CO ₂ / N ₂ separation	[114]
ZIF-8	ZIF-67	Improved capacitance	CAAS	50-4000	170	NA	Supercapacitors	[115]
Au Nanostar	ZIF-8	Immobilization	CAAS	NA	NA	NA	Drug release	[116]

*: Synergy indicates the enhancement either in the selectivity or the reactivity. Immobilization indicates that the main role of MOF is to be a stabilizer, which is also the case for the other roles.

5. Core-shell composites for other applications

5.1 Gas separation

MOFs have been employed intensively for applications in separation mainly due to the high diversity of accessible pore size/shape, along with the possible presence of open metal sites and the possibility to functionalize the ligand.^[117] However, some MOFs suffer from drawbacks such as poor chemical/ physical stability, high capacity but low selectivity or the opposite. Therefore, it would be very useful to combine the functionalities of different MOFs simultaneously. Pioneering works reported by Kitagawa et al. and Rosi et al. on the design of MOF@MOF architectures evidenced the applicability of this strategy.^[8, 118]

Very recently, Shang et al. synthesized a core-shell MOF@MOF structure, in which a Zn-based MOF with 3D structure was chosen as the core (MOF-C) and another Zn-based 2D layered MOF as shell, grown through a competitive ligand exchange method (same concept as ITAS). The structure and morphology of the compound are shown in Figure 18(A-B). Synchrotron X-ray powder diffraction was used to quantify the formation of the core-shell composite as well as the structure conversion from MOF-C (core MOF) to MOF-S (shell MOF). The calculated content of shell could be tuned from 59.9 wt% to 90.2 wt% (Figure 18(C)) upon increase of the ligand exchange time. N₂ sorption isotherms (Figure 18(D)) confirmed the successful fabrication of the core-shell structure. Indeed, the pristine MOF-C showed a typical Type-I isotherm due to its inherent microporosity, while MOF-S and MOF-C@MOF-S both showed a nonporous structure, suggesting the well-formed core-shell structure. CO₂ and N₂ adsorption revealed that the adsorption capacities decreased with the exchange time, in agreement with an increase in the shell thickness that exhibit a much lower N₂ adsorption capacity (Figure 18(E)). Figure 18(F) showed the adsorption selectivity for CO₂ was higher for the core-shell structure than for both the core and the shell, evidencing the synergistic effect of the core-shell architecture.^[114]

In addition, Urban et al. prepared a core-shell structure with a larger pore MOF (UiO-66-NH₂, 0.7nm) as core and smaller pore one (ZIF-8) as shell. The material was used to prepare hybrid membranes presenting a remarkably improved CO₂ separation performance compared to a polysulfone membrane. In this work, the larger pore MOF acted as a molecular transport highway and the small pore MOF shell worked as a molecular filter. This example demonstrated, despite its enhanced complexity compared to single MOF mixed matrix membrane, that the development of MOF-based core-shell could provide new avenues for

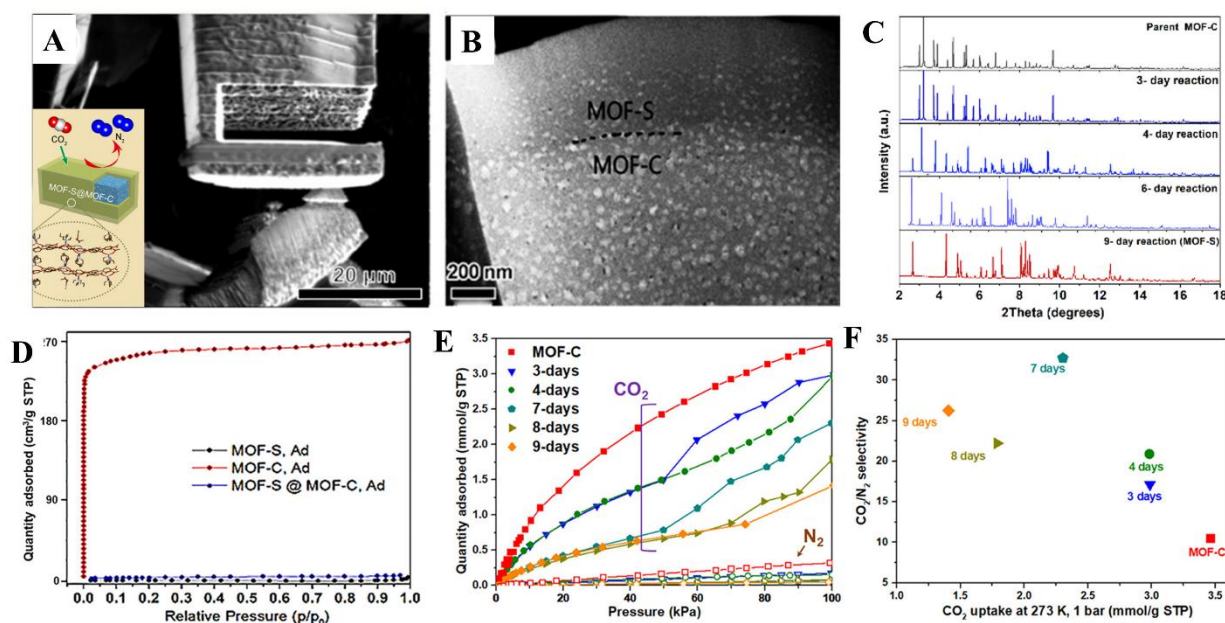


Figure 18. A) SEM image of MOF-C@MOF-S, B) TEM image of a cross section of MOF-C@MOF-S composite. C) Synchrotron X-ray powder diffraction patterns of pristine parent MOF-C and samples with 3-, 4-, 6- (MOF-C@MOF-S) and 9-days (MOF-S) exchange time. D) CO₂ and N₂ adsorption/desorption isotherms and (b) CO₂/ N₂ selectivity and CO₂ uptakes (273 K, 1 bar) of MOF-C@MOF-S with 0- (MOF-C), 3-, 4-, 7-, 8- and 9-days (MOF-S) exchange (N₂, hollow symbols; CO₂, solid symbols). Reproduced with permission.^[114] Copyright 2019, ACS.

Due to the remaining challenges in synthesizing and characterizing well-defined core-shell MOF@MOF architectures, most works reported so far have been barely focused on the synthesis strategies.^[22, 61, 62] However, one can consider gas separation applications using MOF@MOF structures as a promising research domain.

5.2 Sensing

MOFs have been recognized as ideal porous materials for sensing applications, mainly for their tunable physicochemical properties (e.g., optical,^[3] magnetic,^[108] absorptive,^[109] electrical features^[120]). The incorporation of guest species within the MOFs endows wider possibilities for their applications in sensing, such as the enhancement of the optical properties, improvement of the stability of the wrapped species, boosted selectivity towards complex sensing systems, etc. However, core-shell architectures applied in sensing applications are still at their infancy with only few articles reported so far, in which anisotropic or low dimension nano-materials were used.

Fairen-Jimenez et al reported a room temperature strategy to encapsulate thermally sensitive PEG protected plasmonic Au Nanorods (AuNR@PEG-SH) in NU-901, a Zr-based MOF (Figure 19(A-B)). Selective surface-enhanced Raman spectroscopy (SERS) technique was applied to detect 4-mercaptobiphenylcarbonitrile (BPTCN) from varying analyte environments. As shown in Figure 19(C), when separately incubating AuNR@NU-901 in a mixed solution of PST (thiolated polystyrene), PST-BPTCN, BPTCN, and BPT (biphenylthiol), the Raman spectra contains both the MOF peaks and the targeted analyte peaks in the case of BPTCN and MOF, revealing the selective adsorption of BPTCN due to the appropriate size of the molecular and strong affinity of thiols for AuNRs. In an aqueous environment, the characteristic modes at 1091, 1189, and 1588 cm⁻¹ appear in the spectrum

immediately after injection of BPTCN and saturated in 125 s (Figure 19(D)), further evidencing the effective adsorption, as well as the sensitive probing of BPTCN. This work demonstrated the potential of core-shell architecture for Raman-based sensing applications.^[65]

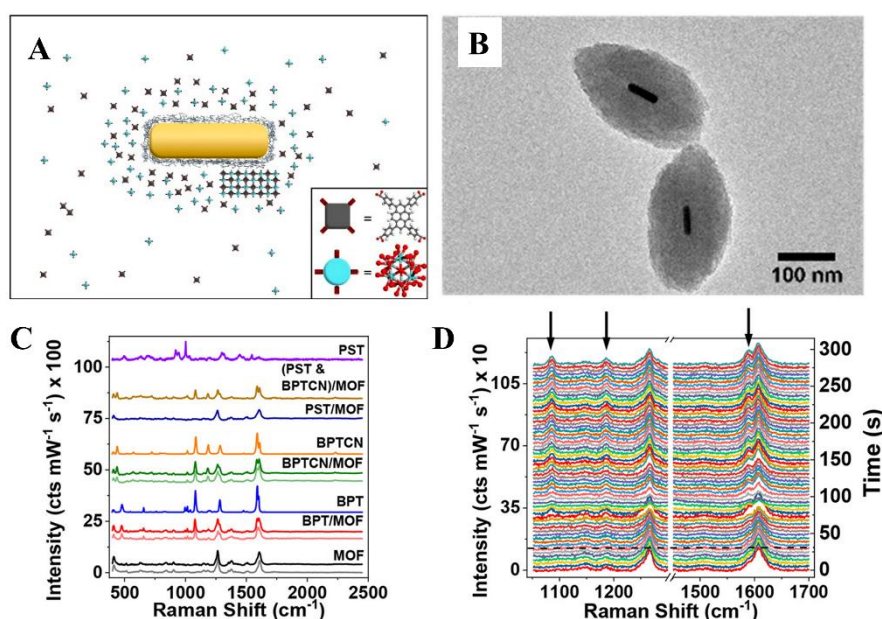


Figure 19. A) Schematic of PEG protected Au nanorods and MOF precursors. B) TEM image of AuNR@NU-901. C) SERS spectra of AuNR@NU-901 before and after incubation with various analytes. D) In situ SERS measurements of BPTCN infiltration in an aqueous environment containing AuNR@NU-901. Reproduced with permission.^[65] Copyright 2019, ACS.

Luminescence is considered as one of the most promising optical properties in sensing applications and several works have reported luminescent species@MOF structures using quantum dots,^[109, 121] or luminescent nanoclusters.^[69, 72] Due to the satisfying biocompatibility of ultra-small nanoclusters, studies already demonstrated their potential in the bio-sensing field.^[122] However, the poor thermal stability of luminescent nanoclusters often hinders the development of this kind of composites as heating is usually needed for the synthesis of most of MOFs. ZIFs appear as an appealing platform for this application due to their chemical robustness and very mild synthesis conditions (e.g., room temperature^[123]). For example, Wang et al. reported the fabrication of a highly luminescent Au Nanoclusters@ZIF-8 composite. The effective encapsulation led to a significant luminescence enhancement in comparison to bare Au nanoclusters (Figure 20A). The obtained luminescent composites showed an interesting selective (Figure 20D, E) and sensitive (Figure 20B, C) detection of H₂S both in liquid and gas phase, although one could point out the risk, upon long term exposure, to disrupt these Zn MOFs through formation of ZnS or to dissolve them through acidification of the media upon formation of H₂SO₄. This example was successfully extended to other luminescent nanoclusters (Ag) and other MOF support (ZIF-7)^[69], which demonstrate the potential of luminescent species@MOF structures for sensing applications. However, we believe there are still a lot of works to perform in order to understand how the host-guest interaction influence the optical properties of the solids and to shape the compounds into sensing devices.

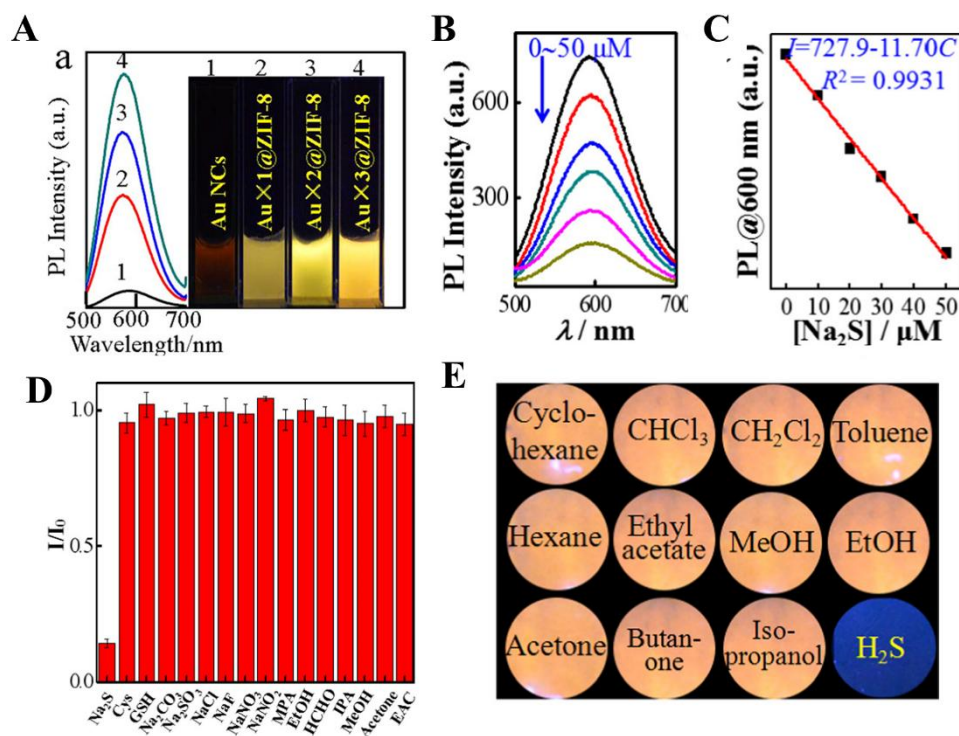


Figure 20. A) Photoluminescence spectra and corresponding photographs of AuNCs, AuNCs \times 1@ZIF-8, AuNCs \times 2@ZIF-8, and AuNCs \times 3@ZIF-8 under 365 nm light. Selective fluorescence sensing of H₂S. B) Photoluminescence intensity evolution, C) and corresponding linear plot of AuNCs \times 3@ZIF-8 in the presence of different concentrations of Na₂S. D) Selectivity tests in the presence of various interferents. E) Photographs of paper sensors exposing to different volatile organic compounds (VOCs) under 365 nm light. Reproduced with permission.^[69] Copyright 2018, ACS.

Other possible applications of MOF-based core-shell architectures are summarized in Table 3.

6. Conclusions and perspectives

In this review, we summarized the recent progresses in the field of MOF-based core-shell composites, mainly including encapsulated inorganic nanoparticles, metal oxides, and MOFs in MOFs. The almost infinite possible combinations, afforded by the massive library of MOFs shells and inorganic materials cores, make these compounds appealing for a wide range of applications. These core-shell composites can combine the advantages of the core materials (properties not present in the shell MOF) and the shell MOFs (designable aperture size/morphologies, physical/ chemical properties), which can ultimately lead to synergetic effects.

Despite the great achievements that have been accomplished to date in this domain, several challenges/ disadvantages still exist. For instance, the use of MOFs with a limited chemical stability as shell is a clear limitation to meet the requirements of practical applications, especially when exposed to water and/or corrosive species. Thus, one important challenge is to further extend these core-shells architectures to more chemically/ thermally robust MOFs, which requires to venture into more complex chemistries that in some cases are not compatible with fragile active species. In addition, the synthetic parameters governing the core-shell formation often remain unclear, even though few reports identified the key roles of

some of them (e.g. capping agent,^[44] anions,^[35] ratio of metal/ ligand,^[65] etc). Systematic explorations of synthetic parameters are still lacking, therefore limiting the successful fabrication of ideal core-shell structures. Indeed, the control of the shell thickness, of the spatial distribution / content of the core remains really challenging, while this is a key parameter in most cases. In addition, the incomplete covering of the core object is sometimes unavoidable, which can negatively influence the overall properties of the core-shell structures. Moreover, the incorporation of small (more active) core materials in a shell framework requires the windows of the shell MOF to be smaller than the size of active NPs to prevent from leaching, particularly when dealing with applications in liquid phase. Thus, such MOFs with narrow pores may be non-porous to large molecules, which can be a potential drawback limiting the size of the reaction substrates. The removal of capping agent is also a key point for more efficient catalysis when performing capping agent-assisted synthesis. However, this step remains almost unexplored due to the difficulty in fully removing the capping agent while maintaining the framework integrity. In addition, it can be quite challenging to characterize the signature of the capping molecule overlapping usually with the signals from the ligand.

In terms of catalytic applications, the charge transfer behavior between metal nodes and NPs can be regarded as a remarkable feature associated with synergetic effects. However, maximizing this interface interaction still requires many efforts. For example, the control of the quantity of guests is not as straightforward in the case of the ship-in-a-bottle synthetic strategy. In addition, the structural parameters allowing an efficient synergy between host and guest remain unclear and additional computational and experimental works are requested to build-up structure-activity correlations that may guide the design of solids with “improved” properties. Finally, the use of a one-pot synthesis strategy should be more developed, as it presents an obvious interest for upscaling the synthesis of such materials. Concomitantly, developing advanced characterization techniques to understand synergetic effects between active NPs and MOF in catalysis is still required in order to better understand the materials’ properties and to guide the design of next generation of solids.

We hope this progress report will shed some light on the current synthesis and characterization of MOF-based core-shell structures that are expanding fast for a broad range of potential applications. It also ambitions to demonstrate that, in order to meet the emerging and challenging demands in various practical applications, developing more facile synthesis strategies and more efficient core-shell composites is still highly desirable.

Acknowledgements

S. D. thanks the support from CSC grant (grant number 201706140196).

Received: ((will be filled in by the editorial staff))

Revised: ((will be filled in by the editorial staff))

Published online: ((will be filled in by the editorial staff))

References

- [1] T. Devic, C. Serre, *Chem. Soc. Rev.* **2014**, 43, 6097; S. Yuan, L. Feng, K. C. Wang, J. D. Pang, M. Bosch, C. Lollar, Y. J. Sun, J. S. Qin, X. Y. Yang, P. Zhang, Q. Wang, L. F. Zou, Y. M. Zhang, L. L. Zhang, Y. Fang, J. L. Li, H. C. Zhou, *Adv. Mater.* **2018**, 30, 1704303; T. Kitao, Y. Y. Zhang, S. Kitagawa, B. Wang, T. Uemura, *Chem. Soc. Rev.* **2017**, 46, 3108.
- [2] M. J. Kalmutzki, N. Hanikel, O. M. Yaghi, *Sci. Adv.* **2018**, 4, eaat9180; H. X. Deng, C. J. Doonan, H. Furukawa, R. B. Ferreira, J. Towne, C. B. Knobler, B. Wang, O. M. Yaghi, *Science* **2010**, 327, 846.

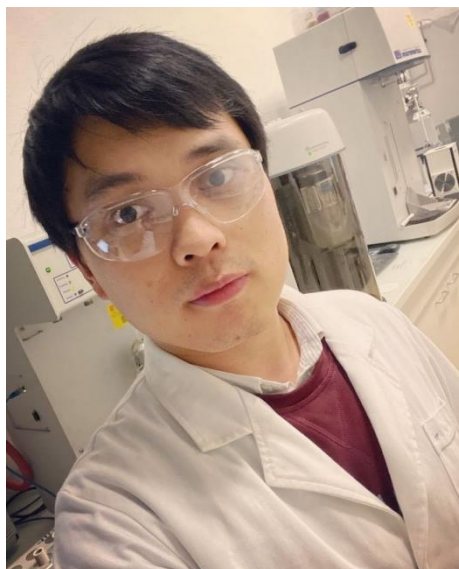
- [3] W. P. Lustig, S. Mukherjee, N. D. Rudd, A. V. Desai, J. Li, S. K. Ghosh, *Chem. Soc. Rev.* **2017**, 46, 3242; H. L. Wang, Q. L. Zhu, R. Q. Zou, Q. Xu, *Chem* **2017**, 2, 52; J. M. Yu, L. H. Xie, J. R. Li, Y. G. Ma, J. M. Seminario, P. B. Balbuena, *Chem. Rev.* **2017**, 117, 9674; T. Simon-Yarza, A. Mielcarek, P. Couvreur, C. Serre, *Adv. Mater.* **2018**, 30, 1870281.
- [4] Q. H. Yang, Q. Xu, H. L. Jiang, *Chem. Soc. Rev.* **2017**, 46, 4774.
- [5] O. K. Farha, I. Eryazici, N. C. Jeong, B. G. Hauser, C. E. Wilmer, A. A. Sarjeant, R. Q. Snurr, S. T. Nguyen, A. O. Yazaydin, J. T. Hupp, *J. Am. Chem. Soc.* **2012**, 134, 15016.
- [6] A. Helal, Z. H. Yamani, K. E. Cordova, O. M. Yaghi, *Nat. Sci. Rev.* **2017**, 4, 296; C. D. Wu, M. Zhao, *Adv. Mater.* **2017**, 29; N. L. Strutt, D. Fairen-Jimenez, J. Iehl, M. B. Lalonde, R. Q. Snurr, O. K. Farha, J. T. Hupp, J. F. Stoddart, *J. Am. Chem. Soc.* **2012**, 134, 17436; T. M. McDonald, D. M. D'Alessandro, R. Krishna, J. R. Long, *Chem. Sci.* **2011**, 2, 2022.
- [7] A. Dhakshinamoorthy, H. Garcia, *Chem. Soc. Rev.* **2012**, 41, 5262; J. Guo, Y. Wan, Y. Zhu, M. Zhao, Z. Tang, *Nano Res.* **2020**, doi.org/10.1007/s12274-020-3182-1.
- [8] T. Li, J. E. Sullivan, N. L. Rosi, *J. Am. Chem. Soc.* **2013**, 135, 9984.
- [9] A. Aijaz, A. Karkamkar, Y. J. Choi, N. Tsumori, E. Ronnebro, T. Autrey, H. Shioyama, Q. Xu, *J. Am. Chem. Soc.* **2012**, 134, 13926; D. Feng, Z. Y. Gu, J. R. Li, H. L. Jiang, Z. Wei, H. C. Zhou, *Angew. Chem., Int. Ed. Engl.* **2012**, 51, 10307.
- [10] G. Lu, S. Li, Z. Guo, O. K. Farha, B. G. Hauser, X. Qi, Y. Wang, X. Wang, S. Han, X. Liu, J. S. DuChene, H. Zhang, Q. Zhang, X. Chen, J. Ma, S. C. Loo, W. D. Wei, Y. Yang, J. T. Hupp, F. Huo, *Nat. Chem.* **2012**, 4, 310.
- [11] X. Z. Lian, Y. Fang, E. Joseph, Q. Wang, J. L. Li, S. Banerjee, C. Lollar, X. Wang, H. C. Zhou, *Chem. Soc. Rev.* **2017**, 46, 3386; R. R. Salunkhe, J. Tang, N. Kobayashi, J. Kim, Y. Ide, S. Tominaka, J. H. Kim, Y. Yamauchi, *Chem. Sci.* **2016**, 7, 5704; R. Canioni, C. Roch-Marchal, F. Secheresse, P. Horcajada, C. Serre, M. Hardi-Dan, G. Ferey, J. M. Greneche, F. Lefebvre, J. S. Chang, Y. K. Hwang, O. Lebedev, S. Turner, G. Van Tendeloo, *J. Mat. Chem.* **2011**, 21, 1226; Y. X. Ye, W. G. Guo, L. H. Wan, Z. Y. Li, Z. J. Song, J. Chen, Z. J. Zhang, S. C. Xiang, B. L. Chen, *J. Am. Chem. Soc.* **2017**, 139, 15604; H. R. Moon, D. W. Lim, M. P. Suh, *Chem. Soc. Rev.* **2013**, 42, 1807.
- [12] A. Aijaz, A. Karkamkar, Y. J. Choi, N. Tsumori, E. Ronnebro, T. Autrey, H. Shioyama, Q. Xu, *J. Am. Chem. Soc.* **2012**, 134, 13926.
- [13] Q. Yang, W. Liu, B. Wang, W. Zhang, X. Zeng, C. Zhang, Y. Qin, X. Sun, T. Wu, J. Liu, F. Huo, J. Lu, *Nat. Commun.* **2017**, 8, 14429.
- [14] H. L. Liu, L. N. Chang, C. H. Bai, L. Y. Chen, R. Luque, Y. W. Li, *Angew. Chem., Int. Edl.* **2016**, 55, 5019.
- [15] T. Tsuruoka, H. Kawasaki, H. Nawafune, K. Akamatsu, *ACS Appl. Mater. Interfaces* **2011**, 3, 3788.
- [16] K. Sugikawa, Y. Furukawa, K. Sada, *Chem. Mater.* **2011**, 23, 3132.
- [17] K. Koh, A. G. Wong-Foy, A. J. Matzger, *Chem. Comm.* **2009**, 6162.
- [18] W. Xia, R. Q. Zou, L. An, D. G. Xia, S. J. Guo, *Energy Environ. Sci.* **2015**, 8, 568.
- [19] S. Ehrling, C. Kutzscher, P. Freund, P. Muller, I. Senkowska, S. Kaskel, *Micropor. Mesopor. Mater.* **2018**, 263, 268.
- [20] K. Shen, L. Zhang, X. Chen, L. Liu, D. Zhang, Y. Han, J. Chen, J. Long, R. Luque, Y. Li, B. *Chem. Sci.* **2018**, 359, 206.
- [21] S. J. Yang, J. Y. Choi, H. K. Chae, J. H. Cho, K. S. Nahm, C. R. Park, *Chem. Mater.* **2009**, 21, 1893.
- [22] F. Wang, S. F. He, H. L. Wang, S. W. Zhang, C. H. Wu, H. X. Huang, Y. Q. Pang, C. K. Tsung, T. Li, *Chem. Sci.* **2019**, 10, 7755.
- [23] C. Y. Guo, J. Guo, Y. H. Zhang, D. Wang, L. Zhang, Y. Guo, W. L. Ma, J. D. Wang, *CrystEngComm* **2018**, 20, 7659.

- [24] H. Kobayashi, Y. Mitsuka, H. Kitagawa, *Inorg. Chem.* **2016**, 55, 7301; Y. Liu, Z. Tang, *Adv. Mater.* **2013**, 25, 5819.
- [25] V. R. Bakuru, S. B. Kalidindi, *Chem. Eur. J.* **2017**, 23, 16456.
- [26] W. Liu, J. Huang, Q. Yang, S. Wang, X. Sun, W. Zhang, J. Liu, F. Huo, *Angew. Chem., Int. Ed. Engl.* **2017**, 56, 5512; X. Deng, S. Liang, X. Cai, S. Huang, Z. Cheng, Y. Shi, M. Pang, P. Ma, J. Lin, *Nano Lett.* **2019**, 19, 6772.
- [27] J. Zhang, J. Wan, J. Wang, H. Ren, R. Yu, L. Gu, Y. Liu, S. Feng, D. Wang, *Angew. Chem., Int. Ed. Engl.* **2019**, 58, 5266.
- [28] L. Wang, J. Wan, Y. Zhao, N. Yang, D. Wang, *J. Am. Chem. Soc.* **2019**, 141, 2238.
- [29] H. Xu, Z. X. Shi, Y. X. Tong, G. R. Li, *Adv. Mater.* **2018**, 30, e1705442.
- [30] F. Meng, S. Zhang, L. Ma, W. Zhang, M. Li, T. Wu, H. Li, T. Zhang, X. Lu, F. Huo, J. Lu, *Adv. Mater.* **2018**, 30, e1803263.
- [31] H. Sheng, D. Chen, N. Li, Q. Xu, H. Li, J. He, J. Lu, *Chem. Mater.* **2017**, 29, 5612.
- [32] X. Zhang, C. Y. Chuah, P. Dong, Y. H. Cha, T. H. Bae, M. K. Song, *ACS Appl. Mater. Interfaces* **2018**, 10, 43316; W. Zhang, Y. Liu, G. Lu, Y. Wang, S. Li, C. Cui, J. Wu, Z. Xu, D. Tian, W. Huang, J. S. DuCheneu, W. D. Wei, H. Chen, Y. Yang, F. Huo, *Adv. Mater.* **2015**, 27, 2923.
- [33] Z. Wang, N. Yang, D. Wang, *Chem. Sci.* **2020**, 11, 5359; Z. Zhao, J. Ding, R. Zhu, H. Pang, *J. Mater. Chem. A* **2019**, 7, 15519; T. Qiu, S. Gao, Z. Liang, D. G. Wang, H. Tabassum, R. Zhong, R. Zou, *Angew. Chem., Int. Ed. Engl.* **2020**, 10.1002/anie.202012699.
- [34] Z. Zheng, H. Xu, Z. Xu, J. Ge, *Small* **2018**, 14, 1702812.
- [35] B. Rungtaweeworanit, J. Baek, J. R. Araujo, B. S. Archanjo, K. M. Choi, O. M. Yaghi, G. A. Somorjai, *Nano Lett.* **2016**, 16, 7645.
- [36] Y. Li, J. Jin, D. Wang, J. Lv, K. Hou, Y. Liu, C. Chen, Z. Tang, *Nano Res.* **2018**, 11, 3294.
- [37] Y. Gu, Y. N. Wu, L. Li, W. Chen, F. Li, S. Kitagawa, *Angew. Chem., Int. Ed. Engl.* **2017**, 56, 15658.
- [38] H. D. Mai, V. C. T. Le, T. M. T. Pham, J.-H. Ko, H. Yoo, *ChemNanoMat* **2017**, 3, 857.
- [39] Z. H. Zhou, M. Y. Li, J. Zhao, Z. G. Di, C. Z. Di, B. Liu, C. Zhang, C. H. Yan, L. L. Li, *Chem. Comm.* **2018**, 54, 8182-8185.
- [40] J. He, R. C. C. Yap, S. Yee Wong, Y. Zhang, Y. Hu, C. Chen, X. Zhang, J. Wang, X. Li, *CrystEngComm* **2016**, 18, 5262; J. J. Zhou, P. Wang, C. X. Wang, Y. T. Goh, Z. Fang, P. B. Messersmith, H. W. Duan, *Acs Nano* **2015**, 9, 6951.
- [41] J.-Y. Zeng, M.-K. Zhang, M.-Y. Peng, D. Gong, X.-Z. Zhang, *Adv. Funct. Mater.* **2018**, 28, 1705451.
- [42] N. R. Jana, L. Gearheart, C. J. Murphy, *Adv. Mater.* **2001**, 13, 1389; T. K. Sau, C. J. Murphy, *J. Am. Chem. Soc.* **2004**, 126, 8648.
- [43] S. Chen, X.-Y. Liu, J. Jin, M. Gao, C. Chen, Q. Kong, Z. Ji, G. A. Somorjai, O. M. Yaghi, P. Yang, *ACS Mater. Lett.* **2020**, 2, 685.
- [44] P. Hu, J. Zhuang, L. Y. Chou, H. K. Lee, X. Y. Ling, Y. C. Chuang, C. K. Tsung, *J. Am. Chem. Soc.* **2014**, 136, 10561.
- [45] J. Zhuang, L. Y. Chou, B. T. Sneed, Y. Cao, P. Hu, L. Feng, C. K. Tsung, *Small* **2015**, 11, 5551.
- [46] K. Wang, N. Li, X. Hai, F. Dang, *J. Mater. Chem. A* **2017**, 5, 20765.
- [47] C. Young, J. Wang, J. Kim, Y. Sugahara, J. Henzie, Y. Yamauchi, *Chem. Mater.* **2018**, 30, 3379.
- [48] W. W. Zhan, Q. Kuang, J. Z. Zhou, X. J. Kong, Z. X. Xie, L. S. Zheng, *J. Am. Chem. Soc.* **2013**, 135, 1926.
- [49] Y. Liu, W. Zhang, S. Li, C. Cui, J. Wu, H. Chen, F. Huo, *Chem. Mater.* **2014**, 26, 1119.

- [50] Y. Zhao, N. Kornienko, Z. Liu, C. Zhu, S. Asahina, T. R. Kuo, W. Bao, C. Xie, A. Hexemer, O. Terasaki, P. Yang, O. M. Yaghi, *J. Am. Chem. Soc.* **2015**, 137, 2199.
- [51] Y. Y. Fu, C. X. Yang, X. P. Yan, *Chemistry* **2013**, 19, 13484.
- [52] B. Li, J. G. Ma, P. Cheng, *Angew. Chem., Int. Ed.* **2018**, 57, 6834.
- [53] M. H. Hassan, D. Andreescu, S. Andreescu, *ACS Appl. Nano Mater.* **2020**, 3, 3288; X. Chen, Y. Zhang, Y. Zhao, S. Wang, L. Liu, W. Xu, Z. Guo, S. Wang, Y. Liu, J. Zhang, *Inorg. Chem.* **2019**, 58, 12433.
- [54] Y. Jiang, X. Zhang, X. Dai, Q. Sheng, H. Zhuo, J. Yong, Y. Wang, K. Yu, L. Yu, C. Luan, H. Wang, Y. Zhu, X. Duan, P. Che, *Chem. Mater.* **2017**, 29, 6336.
- [55] L. He, Y. Liu, J. Liu, Y. Xiong, J. Zheng, Y. Liu, Z. Tang, *Angew. Chem., Int. Ed. Engl.* **2013**, 52, 3741; L. Y. Chen, H. R. Chen, Y. W. Li, *Chem. Comm.* **2014**, 50, 14752.
- [56] D. Li, X. Dai, X. Zhang, H. Zhuo, Y. Jiang, Y.-B. Yu, P. Zhang, X. Huang, H. Wang, *J. Catal.* **2017**, 348, 276.
- [57] P. Á. Szilágyi, M. Lutz, J. Gascon, J. Juan-Alcañiz, J. van Esch, F. Kapteijn, H. Geerlings, B. Dam, R. van de Krol, *CrystEngComm* **2013**, 15; M. Pan, Y. X. Zhu, K. Wu, L. Chen, Y. J. Hou, S. Y. Yin, H. P. Wang, Y. N. Fan, C. Y. Su, *Angew. Chem., Int. Ed. Engl.* **2017**, 56, 14582.
- [58] M. Zhao, K. Yuan, Y. Wang, G. Li, J. Guo, L. Gu, W. Hu, H. Zhao, Z. Tang, *Nature* **2016**, 539, 76.
- [59] K. Choe, F. Zheng, H. Wang, Y. Yuan, W. Zhao, G. Xue, X. Qiu, M. Ri, X. Shi, Y. Wang, G. Li, Z. Tang, *Angew. Chem., Int. Ed. Engl.* **2020**, 59, 3650.
- [60] Y. Yun, H. Sheng, K. Bao, L. Xu, Y. Zhang, D. Astruc, M. Zhu, *J. Am. Chem. Soc.* **2020**, 142, 4126.
- [61] T. Y. Luo, C. Liu, X. Y. Gan, P. F. Muldoon, N. A. Diemler, J. E. Millstone, N. L. Rosi, *J. Am. Chem. Soc.* **2019**, 141, 2161.
- [62] G. Lee, S. Lee, S. Oh, D. Kim, M. Oh, *J. Am. Chem. Soc.* **2020**, 142, 3042.
- [63] O. Kwon, J. Y. Kim, S. Park, J. H. Lee, J. Ha, H. Park, H. R. Moon, J. Kim, *Nat. Commun.* **2019**, 10, 3620.
- [64] X. Yang, S. Yuan, L. Zou, H. Drake, Y. Zhang, J. Qin, A. Alsalmé, H. C. Zhou, *Angew. Chem., Int. Ed. Engl.* **2018**, 57, 3927.
- [65] J. W. M. Osterrieth, D. Wright, H. Noh, C. W. Kung, D. Vulpe, A. Li, J. E. Park, R. P. Van Duyne, P. Z. Moghadam, J. J. Baumberg, O. K. Farha, D. Fairen-Jimenez, *J. Am. Chem. Soc.* **2019**, 141, 3893.
- [66] H. He, L. Li, Y. Liu, M. Kassymova, D. Li, L. Zhang, H.-L. Jiang, *Nano Res.* **2020**, 14, 444.
- [67] S. Dai, F. Nouar, S. Zhang, A. Tissot, C. Serre, *Angew. Chem., Int. Ed. Engl.* **2021**, 60, 4282-4288.
- [68] Z.-W. Zhao, X. Zhou, Y.-N. Liu, C.-C. Shen, C.-Z. Yuan, Y.-F. Jiang, S.-J. Zhao, L.-B. Ma, T.-Y. Cheang, A.-W. Xu, *Catal. Sci. Technol.* **2018**, 8, 3160.
- [69] Q. Gao, S. Xu, C. Guo, Y. Chen, L. Wang, *ACS Appl. Mater. Interfaces* **2018**, 10, 16059.
- [70] W. Zhang, Y. Wang, H. Zheng, R. Li, Y. Tang, B. Li, C. Zhu, L. You, M.-R. Gao, Z. Liu, S.-H. Yu, K. Zhou, *Acs Nano* **2020**, 14, 1971.
- [71] N. Wang, Q. Sun, J. Yu, *Adv. Mater.* **2019**, 31, e1803966.
- [72] Z. G. Wang, R. Chen, Y. Xiong, K. Cepe, J. Schneider, R. Zboril, C. S. Lee, A. L. Rogach, *Part. Part. Syst. Character.* **2017**, 34.
- [73] N. Ogiwara, H. Kobayashi, P. Concepcion, F. Rey, H. Kitagawa, *Angew. Chem., Int. Ed.* **2019**, 58, 11731.
- [74] J. D. Xiao, Q. C. Shang, Y. J. Xiong, Q. Zhang, Y. Luo, S. H. Yu, H. L. Jiang, *Angew. Chem., Int. Ed.* **2016**, 55, 9389.

- [75] N. Ogiwara, H. Kobayashi, M. Inukai, Y. Nishiyama, P. Concepcion, F. Rey, H. Kitagawa, *Nano Lett.* **2020**, 20, 426.
- [76] K. M. Choi, K. Na, G. A. Somorjai, O. M. Yaghi, *J. Am. Chem. Soc.* **2015**, 137, 7810.
- [77] D. P. Schrag, *Science* **2007**, 315, 812.
- [78] J. H. Wu, Y. Huang, W. Ye, Y. G. Li, *Adv. Sci.* **2017**, 4, 1700194
- [79] Y. Han, H. Xu, Y. Su, Z.-l. Xu, K. Wang, W. Wang, *J. Catal.* **2019**, 370, 70.
- [80] X. Zhao, H. T. Xu, X. X. Wang, Z. Z. Zheng, Z. L. Xu, J. P. Ge, *ACS Appl. Mater. Interfaces* **2018**, 10, 15096.
- [81] H. Xu, X. Luo, J. Wang, Y. Su, X. Zhao, Y. Li, *ACS Appl. Mater. Interfaces* **2019**, 11, 20291.
- [82] R. Reske, H. Mistry, F. Behafarid, B. Roldan Cuenya, P. Strasser, *J. Am. Chem. Soc.* **2014**, 136, 6978; B. An, Z. Li, Y. Song, J. Zhang, L. Zeng, C. Wang, W. Lin, *Nat. Catal.* **2019**, 2, 709.
- [83] Y. Dou, J. Zhou, A. Zhou, J.-R. Li, Z. Nie, *J. Mater. Chem. A* **2017**, 5, 19491.
- [84] D. W. Flaherty, W. Y. Yu, Z. D. Pozun, G. Henkelman, C. B. Mullins, *J. Catal.* **2011**, 282, 278.
- [85] J. D. Xiao, H. L. Jiang, *Acc. Chem. Res.* **2019**, 52, 356; J. H. Qiu, X. G. Zhang, Y. Feng, X. F. Zhang, H. T. Wang, J. F. Yao, *Appl. Catal. B-Environ.* **2018**, 231, 317.
- [86] B. Wu, H. Huang, J. Yang, N. Zheng, G. Fu, *Angew. Chem., Int. Ed. Engl.* **2012**, 51, 3440.
- [87] Z. Tian, X. Xiang, L. Xie, F. Li, *Ind. Eng. Chem. Res.* **2012**, 52, 288.
- [88] N. Zhang, Q. Shao, P. Wang, X. Zhu, X. Huang, *Small* **2018**, 14, e1704318.
- [89] R. T. Tung, *Appl. Phys. Rev.* **2014**, 1, 54; Y. Liu, J. Guo, E. B. Zhu, L. Liao, S. J. Lee, M. N. Ding, I. Shakir, V. Gambin, Y. Huang, X. F. Duan, *Nature* **2018**, 557, 696.
- [90] N. Tsumori, L. Chen, Q. Wang, Q.-L. Zhu, M. Kitta, Q. Xu, *Chem.* **2018**, 4, 845.
- [91] V. R. Bakuru, B. Velaga, N. R. Peela, S. B. Kalidindi, *Chemistry* **2018**, 24, 15978.
- [92] J. Li, H. Gao, L. Tan, Y. Luan, M. Yang, *Eur. J. Inorg. Chem.* **2016**, 30, 4906.
- [93] H. Gao, Y. Luan, K. Chaikittikul, W. Dong, J. Li, X. Zhang, D. Jia, M. Yang, G. Wang, *ACS Appl. Mater. Interfaces* **2015**, 7, 4667.
- [94] J. Wang, H. Xu, C. Ao, X. Pan, X. Luo, S. Wei, Z. Li, L. Zhang, Z. L. Xu, Y. Li, *iScience* **2020**, 23, 101233.
- [95] H. Zhang, H. Xu, Y. Li, Y. Su, *Appl. Mater. Today* **2020**, 19, 100609.
- [96] F. Zhang, X. Hu, E. W. Roth, Y. Kim, S. T. Nguyen, *Chem. Mater.* **2020**, 32, 4292.
- [97] X. Li, Z. Zhang, W. Xiao, S. Deng, C. Chen, N. Zhang, *J. Mater. Chem. A* **2019**, 7, 14504.
- [98] Y. Wang, L. Ling, W. Zhang, K. Ding, Y. Yu, W. Duan, B. Liu, *ChemSusChem* **2018**, 11, 666.
- [99] M. Zeng, Z. Chai, X. Deng, Q. Li, S. Feng, J. Wang, D. Xu, *Nano Res.* **2016**, 9, 2729.
- [100] Y. Gong, Y. Yuan, C. Chen, P. Zhang, J. Wang, A. Khan, S. Zhuiykov, S. Chaemchuen, F. Verpoort, *J. Catal.* **2019**, 375, 371.
- [101] A. Zhou, Y. Dou, J. Zhou, J. R. Li, *ChemSusChem* **2020**, 13, 205.
- [102] Y. Gong, Y. Yuan, C. Chen, P. Zhang, J. Wang, S. Zhuiykov, S. Chaemchuen, F. Verpoort, *J. Catal.* **2019**, 371, 106.
- [103] L. Li, W. Yang, Q. Yang, Q. Guan, J. Lu, S.-H. Yu, H.-L. Jiang, *ACS Catal.* **2020**, 10, 7753.
- [104] R. Ma, P. Yang, Y. Ma, F. Bian, *ChemCatChem* **2018**, 10, 1446.
- [105] L. Chen, W. Zhan, H. Fang, Z. Cao, C. Yuan, Z. Xie, Q. Kuang, L. Zheng, *Chemistry* **2017**, 23, 11397.
- [106] Y. Long, S. Song, J. Li, L. Wu, Q. Wang, Y. Liu, R. Jin, H. Zhang, *ACS Catal.* **2018**, 8, 8506.

- [107] L. Chen, H. Li, W. Zhan, Z. Cao, J. Chen, Q. Jiang, Y. Jiang, Z. Xie, Q. Kuang, L. Zheng, *ACS Appl. Mater. Interfaces* **2016**, 8, 31059.
- [108] K. Sun, M. Liu, J. Pei, D. Li, C. Ding, K. Wu, H. L. Jiang, *Angew. Chem., Int. Ed.* **2020**, 59, 22749-22755.
- [109] F. Asadi, S. N. Azizi, M. J. Chaichi, *Mater. Sci. Eng. C* **2019**, 105, 110058.
- [110] Y. Li, J. Tang, L. He, Y. Liu, Y. Liu, C. Chen, Z. Tang, *Adv. Mater.* **2015**, 27, 4075-4080.
- [111] W. Shang, C. Zeng, Y. Du, H. Hui, X. Liang, C. Chi, K. Wang, Z. Wang, J. Tian, *Adv. Mater.* **2017** 2017, 29.
- [112] K. M. Choi, J. H. Park, J. K. Kang, *Chem. Mater.* **2015**, 27, 5088.
- [113] L. Zhang, J. Wang, X. Ren, W. Zhang, T. Zhang, X. Liu, T. Du, T. Li, J. Wang, *J. Mater. Chem. A* **2018**, 6, 21029.
- [114] Y. He, M. Sun, Q. Zhao, J. Shang, Y. Tian, P. Xiao, Q. Gu, L. Li, P. A. Webley, *ACS Appl. Mater. Interfaces* **2019**, 11, 30234.
- [115] J. Tang, R. R. Salunkhe, J. Liu, N. L. Torad, M. Imura, S. Furukawa, Y. Yamauchi, *J. Am. Chem. Soc.* **2015**, 137, 1572.
- [116] C. Carrillo-Carrion, R. Martinez, M. F. N. Poupard, B. Pelaz, E. Polo, A. Arenas-Vivo, A. Olgiati, P. Taboada, M. G. Soliman, U. Catalan, S. Fernandez-Castillejo, R. Sola, W. J. Parak, P. Horcajada, R. A. Alvarez-Puebla, P. del Pino, *Angew. Chem., Int. Ed.* **2019**, 58, 7078.
- [117] K. Adil, Y. Belmabkhout, R. S. Pillai, A. Cadiau, P. M. Bhatt, A. H. Assen, G. Maurin, M. Eddaoudi, *Chem. Soc. Rev.* **2017**, 46, 3402.
- [118] S. Furukawa, K. Hirai, K. Nakagawa, Y. Takashima, R. Matsuda, T. Tsuruoka, M. Kondo, R. Haruki, D. Tanaka, H. Sakamoto, S. Shimomura, O. Sakata, S. Kitagawa, *Angew. Chem., Int. Ed. Engl.* **2009**, 48, 1766.
- [119] Z. Song, F. Qiu, E. W. Zaia, Z. Wang, M. Kunz, J. Guo, M. Brady, B. Mi, J. J. Urban, *Nano Lett.* **2017**, 17, 6752.
- [120] M. G. Campbell, D. Sheberla, S. F. Liu, T. M. Swager, M. Dinca, *Angew. Chem., Int. Ed.* **2015**, 54, 4349.
- [121] K. Wang, N. Li, J. Zhang, Z. Zhang, F. Dang, *Biosens. Bioelectron.* **2017**, 87, 339.
- [122] F. Cao, E. Ju, C. Liu, W. Li, Y. Zhang, K. Dong, Z. Liu, J. Ren, X. Qu, *Nanoscale* **2017**, 9, 4128.
- [123] J. Cravillon, R. Nayuk, S. Springer, A. Feldhoff, K. Huber, M. Wiebcke, *Chem. Mater.* **2011**, 23, 2130; Y. C. Pan, Y. Y. Liu, G. F. Zeng, L. Zhao, Z. P. Lai, *Chem. Comm.* **2011**, 47, 2071.



Shan Dai obtained his bachelor degree in 2015 from HeFei University of Technology and joined the “PROSFER” (Programme of Sino-French Education for Research) in East China Normal University. He started his PhD from 2017 in École Normale Supérieure (ENS). His research interests focus on the development of novel green/ scalable synthesis methods for chemically stable MOFs and the constructions of hybrid Metal Nanoparticles@Metal-organic Frameworks composites for catalysis applications.



Antoine Tissot is a CNRS researcher at the Porous Materials Institute of Paris. Following his PhD in coordination chemistry dedicated to the study of molecular spin crossover nanocrystals at University Paris-Sud, he stayed at University of Geneva Hauser as a postdoctoral researcher where he studied photophysics of coordination compounds. He was then recruited as CNRS researcher in the Institut Lavoisier de Versailles in 2014 and moved to the newly created Porous Materials Institute of Paris in September 2016. He is currently working on the synthesis and functionalization of Metal Organic Frameworks for applications in sensing, catalysis and conductivity.



Christian Serre is a CNRS research director. Previously leading the Porous Solids team from Institut Lavoisier de Versailles (France), and one of the founders of the MIL-n MOF materials, Christian created in 2016 the Institute of Porous Materials at the Ecole Normale Supérieure and ESPCI Paris within PSL university (France). His research interests lie in the discovery of robust metal-organic frameworks and related composites and their potential applications in energy, environment and health